



ELSEVIER

Contents lists available at ScienceDirect

Journal of the Mechanics and Physics of Solids

journal homepage: www.elsevier.com/locate/jmps

Modeling of crack tip fields and fatigue crack growth in fcc crystals

Baolin Wang, Yin Zhang, David L. McDowell, Ting Zhu*

Woodruff School of Mechanical Engineering, Georgia Institute of Technology, Atlanta, GA, 30332, USA

ARTICLE INFO

Keywords:

Crack tip field
Fatigue crack growth
Cyclic crystal plasticity finite element modeling
Metal alloys

ABSTRACT

Predicting the mechanical behavior of polycrystalline materials containing a crack under both monotonic and cyclic loading conditions is crucial for accurately assessing the integrity of engineering materials. This study focuses on the deformation characteristics of face-centered cubic (fcc) grains within the crack tip field and their significant role in governing the driving force for fatigue crack growth during cyclic loading. We employ a cyclic crystal plasticity finite element (CPFE) model to analyze the mechanical response of austenitic 316L stainless steel polycrystals by accounting for nonlinear kinematic hardening effects. Through CPFE simulations, we investigate the deformation fields in 316L grains at the crack tip, considering two different grain orientations under plane strain conditions. Our CPFE results under monotonic loading align consistently with previous theoretical and experimental findings, particularly in comparing CPFE-simulated and experimentally observed plastic sectors consisting of different slip traces on the specimen surface near the crack tip. Based on a critical plastic work criterion for crack advancement, cyclic CPFE simulations are used to determine the fatigue crack growth rate as a function of stress intensity factor range for the two crack tip grain orientations in stainless steel. The simulated Paris law exponent matches experimental values. Furthermore, we compare cyclic CPFE results with those from cyclic J_2 plasticity finite element simulations. This study demonstrates a cyclic CPFE approach for determining crack tip fields, accounting for crystallographic effects on plastic deformation of crack tip grains. Our approach can be applied to effectively evaluate fatigue crack growth rates in fcc polycrystalline metals.

1. Introduction

Assessing the integrity of engineering materials often requires the predictive modeling of mechanical behavior of polycrystalline materials containing a crack under both monotonic and cyclic loading conditions (Suresh, 1998). While extensive experimental and modeling research has been conducted to investigate crack tip fields and fatigue crack growth rates in the past, there remains a critical need for computational models with the capability to analyze deformation fields within crack tip grains and evaluate their influence on fatigue crack growth rates during cyclic loading. This study focuses on developing a cyclic crystal plasticity finite element (CPFE) approach for determining crack tip deformation fields and fatigue crack growth rates in crystalline solids, which can be significantly influenced by the crystallographic effects of grains within the crack tip field. Below, we provide an overview of previous theoretical,

This paper is dedicated to the special issue in honor of Prof. Wei Yang on the occasion of his 70th birthday.

* Corresponding author.

E-mail address: ting.zhu@me.gatech.edu (T. Zhu).

<https://doi.org/10.1016/j.jmps.2024.105691>

Received 19 December 2023; Received in revised form 14 April 2024; Accepted 18 May 2024

Available online 19 May 2024

0022-5096/© 2024 Elsevier Ltd. All rights are reserved, including those for text and data mining, AI training, and similar technologies.

computational and experimental studies of crack tip deformation fields and fatigue crack growth rates with an emphasis on the crystallographic effects of crack tip grains.

Theoretical studies of crack tip deformation fields inside single crystals and polycrystals have been reported in the literature. Rice (Rice, 1987) conducted an asymptotic analysis of crack tip deformation fields for two orthogonal symmetric crack orientations under mode I loading and plane strain conditions in ideally plastic single crystals. His asymptotic solution for each crack orientation consists of four angular sectors near the stationary crack tip with a constant stress state in each sector, featuring a slip-type or kink-type concentrated plastic deformation band at sector boundaries. Rice pointed out that under small strain deformation, cracks with these two orthogonal orientations in both face-centered cubic (fcc) and body-centered cubic (bcc) crystals have identical deformation fields near a crack tip. Subsequently, (Saeedvafa and Rice (1989) studied single crystals with power-law hardening. They presented an asymptotic solution of the HRR type (Hutchinson, 1968; Rice and Rosengren, 1968) for cracks with the same orientations as Rice's earlier work (Rice, 1987). The solutions by Saeedvafa and Rice show more complex stress distributions and sectors with different active slip systems and are able to converge to Rice's earlier solution (Rice, 1987) in the limit of infinitesimal hardening. (Drugan, 2001) extended Rice's analysis by introducing sub-yield near tip sectors to obtain an asymptotic solution without kink-type concentrated plastic deformation bands. His solution is more consistent with experimental observations (Shield, 1996; Shield and Kim, 1994) and discrete dislocation dynamics simulations (Cleveringa et al., 2000; Nakatani et al., 1999; Van der Giessen et al., 2001) for the two symmetric crack orientations. Patil et al. (Patil et al., 2009) generalized the asymptotic solutions to account for the effect of triaxiality.

Numerical studies have been performed to analyze crack tip fields in single crystals with the two crack orientations studied by Rice with asymptotic solutions (Rice, 1987). For example, (Rice et al., 1990) conducted a two-dimensional (2D) finite element (FE) analysis to simulate the crack tip fields in single crystals under small strain and small scale yielding conditions. They found that the FE results are consistent with the earlier asymptotic solution (Rice, 1987). (Mohan et al., 1992) performed FE simulations of mode I cracks in single crystals with an experimentally based hardening response. In their work, finite deformation is considered by a geometrically rigorous formulation. The results are in partial agreement with the earlier asymptotic (Rice, 1987) and numerical solutions (Rice et al., 1990). Cuitino and Ortiz developed a crystal plasticity (CP) model, and they performed CP finite element (CPFE) simulations to obtain 2D crack tip fields in tensile single-crystal specimens (Cuitino and Ortiz, 1993) and three-dimensional (3D) crack tip fields in single crystal specimens under four point bending (Cuitino and Ortiz, 1996). Their CPFE solution of a mode I crack (Cuitino and Ortiz, 1993) agrees closely with Rice's solution (Rice, 1987) in regions where strains and lattice rotations are small. However, they found more activated slip systems in the near-tip region. In the 3D study of cracks in four-point-bending specimens (Cuitino and Ortiz, 1996), they observed different patterns of slip activity at the surface and in the interior of the specimen. Forest et al. (2001) and Flouriot et al. (2003a) studied strain localization patterns at the crack tip of compact tension (CT) specimens. Forest et al. (2001) found that the introduction of hardening suppresses kink banding due to lattice curvature effects and promotes slip banding. Flouriot et al. (2003a) carried out 3D FE simulations for three crack orientations and found good agreement between numerical and experimental results of the strain band structure. Patil et al. (2008a) considered crack tip fields in a single edge notched specimen in both experimental and computational studies. They used a CP model with an isotropic hardening rule (Peirce et al., 1983), and their CPFE results of localized strain bands are in good agreement with experimental observations.

Experimental studies have been conducted to investigate plastic deformation and strain localization near the crack tip by Shield and his colleagues (Crone and Shield, 2001; Crone et al., 2004, 2003; Shield, 1996; Shield and Kim, 1994). They used the Moire method to measure surface strain fields in iron-silicon, copper, and copper-beryllium single crystals loaded by four-point bending (Crone and Shield, 2001; Shield, 1996; Shield and Kim, 1994). These investigations generally showed good agreement with Rice's analysis, but several discrepancies were also reported. For instance, an elastic sector where surface strains show approximately $1/r$ singularity was observed, with r being a radial distance from the crack tip (Shield, 1996; Shield and Kim, 1994). This finding was accounted for in Drugan's asymptotic analysis (Drugan, 2001). They found that strain fields develop in a nonproportional manner, and the sector containing the most plastic deformation shifts as the applied load increases (Shield, 1996). Experimental results of crack tip fields (Crone and Shield, 2001; Shield, 1996; Shield and Kim, 1994) for two orthogonal crack orientations differed from each other, which contrasted with the identical crack tip fields in Rice's work (Rice, 1987). This difference indicates that the assumption of interchangeable slip and kink directions is not applicable in experiments. Crone and Shield (Crone and Shield, 2003) further investigated the effect of strain hardening on plastic deformation fields near the crack tip in ductile single crystals and showed that the experimental results are in better agreement with Drugan's solution (Drugan, 2001) than Rice's solution (Rice, 1987). Crone et al. (2004) studied the orientation dependence of plastic deformation fields near crack tips in ductile fcc single crystals by testing two symmetric crystallographic orientations and four nonsymmetric crystallographic orientations. They identified sectors with a similar pattern of slip activity and analyzed different types of sector boundaries. Kysar and Briant (2002) studied crack tip deformation fields in aluminum single crystals subjected to mode I loading through electron backscatter diffraction (EBSD) experiments and observed kink sector boundaries predicted by Rice's solution (Rice, 1987). Patil et al. (2008a) and Flouriot et al. (2003a) also confirmed the existence of kink bands near the crack tip in ductile single crystals through EBSD analyses.

The crack tip deformation fields in single crystals under cyclic loading have also been studied by experiments (McEvily and Boettner, 1963; Vehoff and Neumann, 1979) and numerical simulations (Deka and Jonnalagadda, 2017; Flouriot et al., 2003b; Marchal et al., 2006; Zirkle and McDowell, 2022). (McEvily and Boettner, 1963) observed crack growth in single crystals of aluminum, polycrystalline copper and a series of polycrystalline copper alloys to investigate the mechanism of fatigue crack growth. Vehoff and Neumann (1979) observed growing fatigue cracks in copper and Fe-2.4 %Si single crystals during cyclic loading inside a scanning electron microscope. Both studies showed slip localization near crack tips and found that slip localization plays an important role in the crack growth rate and crack path. Inspired by these experimental observations and numerical studies of crack tip fields in single crystals under monotonic loading, CPFE simulations were conducted to study crack tip strain localization under cyclic loading in single

crystals. [Flouriot et al. \(2003b\)](#) used a non-linear kinematic hardening model ([Armstrong and Frederick, 1966](#)) to explore the evolution of plastic strain near the crack tip in a CT specimen subjected to cyclic loading. They observed plastic strain localization bands and noted that plastic strain accumulated more significantly in the forward direction at the crack tip and referred to this phenomenon as ratchetting. [Marchal et al. \(2006\)](#) applied a “crystallographic phenomenological” model to examine the crack tip stress and strain fields in single crystal nickel-base superalloys subjected to creep-fatigue loading at high temperatures. They found two slip bands accumulating over cycles. [Deka and Jonnalagadda \(2017\)](#) combined isotropic and Armstrong and Frederick kinematic hardening laws to investigate the cyclic stress and strain behavior near a crack tip. Plastic strain was observed to predominantly accumulate along a particular slip band, similar to the result of [Flouriot et al. \(2003b\)](#). [Zirkle and McDowell \(2022\)](#) used a CPFE model that takes into account the evolution of dislocation substructures and associated back stresses to study a stationary crack in fcc single crystals under monotonic and cyclic loading. Their CPFE simulations revealed the development of alternating forward and reverse shear strain localization bands at the crack tip.

Fatigue crack growth is a common failure mode in crystalline materials under cyclic loading. The fatigue crack growth rate is often used to estimate fatigue life in engineering applications. Early studies modeled the fatigue crack growth rate based on a cumulative damage criterion for crack advancement ([Liu and Iino, 1969](#); [Majumdar and Morrow, 1974](#)) within some damage process zone at the crack tip. For example, an indicator of damage accumulation has often been used as a fatigue crack growth criterion. Fatigue ductility ([Oh, 1978](#)), plastic strain ([Glinka, 1982](#); [Radon, 1982](#)), and cyclic strain energy density ([Jiang, 2000](#); [Kujawski and Ellyin, 1984](#); [Majumdar and Morrow, 1974](#); [Morrow, 1965](#)) have also been used as indicators for fatigue crack growth, effectively serving as surrogate measures for the cyclic driving force. Fundamentally, fatigue crack growth is related to the irreversibility of the cyclic crack tip displacement (ΔCTD) that is vectorially comprised of the cyclic crack tip opening displacement ($\Delta CTOD$) and cyclic crack tip sliding displacement ($\Delta CTS D$). Hence, the magnitude of the fatigue crack growth rate is the fraction of the ΔCTD that is not reversed during the cycle, representing cyclic crack extension. Fatigue indicator parameters (FIPs) such as the Fatemi-Socie FIP ([Fatemi and Socie, 1988](#)) based on the maximum cyclic plastic shear strain and the peak normal stress on the maximum plastic shear range plane have been used to determine fatigue crack growth. [Castelluccio and McDowell \(2012\)](#) evaluated a crystallographic form of the Fatemi-Socie FIP averaged over some finite band ahead of the crack tip as a coarse-grained surrogate measure for the ΔCTD and showed that these two parameters are correlated and interchangeable in serving as a driving force for multiple loading conditions. [Sakaguchi et al. \(2019\)](#) used the modified Fatemi-Socie FIP in a CPFE analysis and correlated this parameter to experimentally measured crack growth rates. Recently, [Hosseini et al. \(2018\)](#) developed an FE methodology to determine the fatigue crack growth rate in ductile materials. Crack propagation was modeled by nodal release when the accumulated plastic work density in the crack tip element reached a critical value. [Karamitros et al. \(2022\)](#) conducted CP and extended finite element analyses of edge-cracked Ni-based superalloy single crystals, and they determined crack growth rates using the critical stored energy density as an indicator of damage accumulation. The simulated fatigue crack growth rates are consistent with experimentally measured values from specimens with different orientations.

Among the numerical simulations reviewed above, excepting the work of McDowell et al. ([Castelluccio and McDowell, 2012, 2014a](#); [Castelluccio and McDowell, 2014b](#); [Castelluccio et al., 2014](#); [Hennessey et al., 2017](#)), crack tip stress and strain fields in single crystals were typically determined using CP models that neglect kinematic hardening effects or employing a J_2 -based Armstrong and Frederick kinematic hardening law, which tends to overestimate the accumulation of ratcheting strain over cycles with a positive stress ratio ([McDowell, 1995](#); [Ohno and Wang, 1993](#)). While there has been an increased focus on studying fatigue crack growth using CP models in recent years ([Aslan et al., 2011](#); [Karamitros et al., 2022](#); [Sakaguchi et al., 2019](#)), crack tip fields have not been systematically examined under cyclic loading conditions. In addition, only a limited number of numerical simulations have addressed fatigue crack growth in single crystals or polycrystals subjected to cyclic loading.

In this work, we employ a CPFE approach to investigate the stress and strain fields near a stationary crack in 316L stainless steel under both monotonic and cyclic loading conditions. To account for the pronounced Bauschinger effect in 316L stainless steel under cyclic loading conditions ([Pham et al., 2013](#)), a nonlinear kinematic hardening law with multiple back stress terms is incorporated at the slip system level into a finite deformation CP framework. We combine cyclic CPFE simulations with a critical plastic work criterion, based on integrated plastic work over cycles within the plastic zone of a stationary crack, to evaluate fatigue crack growth rates following the Paris law ([Paris and Erdogan, 1963](#)). For comparison, we use cyclic J_2 plasticity FE (JPFE) simulations to determine fatigue crack growth rates, also following the Paris law. Furthermore, the Paris law exponents obtained from JPFE and CPFE simulations are compared with experimental values. Overall, this study demonstrates a cyclic CPFE approach for determining crack tip fields, accounting for the crystallographic effects of crack tip grains on plastic deformation. Such an approach can be applied to effectively evaluate fatigue crack growth rates in fcc polycrystalline metals.

2. Methods

2.1. Cyclic J_2 plasticity model

A rate-independent cyclic J_2 plasticity (JP) model is employed to simulate the elastic-plastic behavior of materials under cyclic loading. The yield surface is described by the von Mises yield criterion

$$f = \sigma_e - \sigma_Y = 0 \quad (1)$$

where σ_Y is the size of the yield surface and σ_e is the Mises equivalent stress

$$\sigma_e = \sqrt{\frac{3}{2}(\mathbf{S} - \boldsymbol{\alpha}') : (\mathbf{S} - \boldsymbol{\alpha}')} \quad (2)$$

In Eq. (2), \mathbf{S} is the deviatoric stress tensor given by $\mathbf{S} = \boldsymbol{\sigma} - p\mathbf{I}$, where $\boldsymbol{\sigma}$ is the Cauchy stress tensor, \mathbf{I} is the identity tensor, $p = \sigma_{kk}/3$ is the hydrostatic stress and repeated indices imply summation; and $\boldsymbol{\alpha}'$ is the deviatoric part of the back stress tensor $\boldsymbol{\alpha}$.

The plastic strain rate tensor $\dot{\boldsymbol{\epsilon}}^p$ is given by

$$\dot{\boldsymbol{\epsilon}}^p = \dot{\bar{\epsilon}}^p \frac{\partial f}{\partial \boldsymbol{\sigma}} \quad (3)$$

where $\dot{\bar{\epsilon}}^p = \sqrt{\frac{2}{3}\dot{\boldsymbol{\epsilon}}^p : \dot{\boldsymbol{\epsilon}}^p}$ is the effective plastic strain rate. The effective plastic strain $\bar{\epsilon}^p$ is obtained by $\bar{\epsilon}^p = \int \dot{\bar{\epsilon}}^p dt$. The plastic work rate is the product of the Mises stress and effective plastic strain rate or equivalently the product of the stress and plastic strain rate tensors

$$\sigma_e \dot{\bar{\epsilon}}^p = \boldsymbol{\sigma} : \dot{\boldsymbol{\epsilon}}^p \quad (4)$$

The evolution of the yield surface is represented by a kinematic hardening rule that describes the translation of the yield surface induced by the back stress tensor $\boldsymbol{\alpha}$ as well as an isotropic hardening rule that describes the expansion of the yield surface. The nonlinear kinematic hardening model by Chaboche (1986) is adopted, and it involves the superposition of three Armstrong-Frederick terms. Each of these terms represents nonlinear hardening behavior for a certain range of strain in the stress-strain hysteresis loop (Bari and Hassan, 2000; Hassan and Kyriakides, 1992). Thus, the Chaboche model effectively represents most prominent cyclic stress-strain characteristics (Chaboche, 1991). More specifically, the back stress tensor $\boldsymbol{\alpha}$ consists of three components, $\boldsymbol{\alpha} = \boldsymbol{\alpha}_1 + \boldsymbol{\alpha}_2 + \boldsymbol{\alpha}_3$. The rate of back stress $\dot{\boldsymbol{\alpha}}_k$ is expressed as

$$\dot{\boldsymbol{\alpha}}_k = C_k \frac{1}{\sigma_Y} (\boldsymbol{\sigma} - \boldsymbol{\alpha}) \dot{\bar{\epsilon}}^p - D_k \boldsymbol{\alpha}_k \dot{\bar{\epsilon}}^p, \quad k = 1, 2, 3 \quad (5)$$

where C_k and D_k are the material parameters associated with $\boldsymbol{\alpha}_k$.

To represent the hardening behavior of σ_Y , a non-linear exponential law is used

$$\sigma_Y = \sigma_{Y0} + Q_\infty (1 - e^{-b\bar{\epsilon}^p}) \quad (6)$$

where σ_{Y0} is the yield surface size at zero plastic strain, Q_∞ is the maximum size increase of the yield surface, and b is the rate of increase of the yield surface with $\bar{\epsilon}^p$.

2.2. Cyclic crystal plasticity model

A cyclic CP model is developed to represent the elastic-viscoplastic behavior of crystal grains under cyclic loading. This model extends the CP framework of Asaro and Needleman (Asaro and Needleman, 1985) and Kalidindi et al. (1992) to account for nonlinear kinematic hardening at the slip system level, akin to the J_2 kinematic hardening model by Chaboche (1986). Despite the viscoplastic formulation used, the strain rate sensitivity is small for the coarse-grained stainless steel studied. Consequently, the simulated cyclic viscoplastic response approaches its rate-independent counterpart from the cyclic JP model in Section 2.1.

In the continuum mechanics framework for finite deformation, the deformation gradient tensor \mathbf{F} can be decomposed into its elastic \mathbf{F}^e and plastic \mathbf{F}^p parts such that $\mathbf{F} = \mathbf{F}^e \mathbf{F}^p$. The rate of plastic deformation gradient is given by

$$\dot{\mathbf{F}}^p = \mathbf{L}^p \mathbf{F}^p \quad (7)$$

The plastic velocity gradient \mathbf{L}^p is

$$\mathbf{L}^p = \sum_\alpha \dot{\gamma}^\alpha \mathbf{S}_0^\alpha \quad (8)$$

where $\mathbf{S}_0^\alpha = \mathbf{m}_0^\alpha \otimes \mathbf{n}_0^\alpha$, with \mathbf{m}_0^α and \mathbf{n}_0^α being the unit vectors corresponding to the slip direction and slip plane normal direction of slip system α in the reference configuration, respectively, and $\dot{\gamma}^\alpha$ is the plastic shearing rate on slip system α . Each fcc grain consists of 12 $\{111\}\langle 110 \rangle$ slip systems.

The applied resolved shear stress (RSS) acting on slip system α is expressed as

$$\tau^\alpha = (\mathbf{C}^* \mathbf{T}^*) : \mathbf{S}_0^\alpha \quad (9)$$

In Eq. (9), $\mathbf{C}^* = \mathbf{F}^{*T} \mathbf{F}^*$ is the right Cauchy-Green tensor and $\mathbf{T}^* = \mathbf{F}^{*-1} \{(\det \mathbf{F}^*) \boldsymbol{\sigma}\} \mathbf{F}^{*-T}$ is the second Piola-Kirchhoff stress tensor. The elastic stretch is usually infinitesimal for metallic materials, so that $\tau^\alpha \approx \mathbf{T}^* : \mathbf{S}_0^\alpha$ (Kalidindi et al., 1992).

Two resolved back stress components are introduced to account for kinematic hardening at the slip system level. The rate of the resolved back stress is

$$\dot{B}_i^\alpha = \tilde{C}_i \dot{\gamma}^\alpha - \tilde{D}_i B_i^\alpha |\dot{\gamma}^\alpha|, \quad i = 1, 2 \quad (10)$$

where B_i^α is the i -th component of the resolved back stress on slip system α , and \tilde{C}_i and \tilde{D}_i are the material parameters. While Eq. (10) is sufficient to capture the cyclic plastic strain response of stainless steel, Hennessey et al. (Hennessey et al., 2017) showed that for 7075-T6 Al it was necessary to employ a nonlinear dynamic recovery term as opposed to the linear one in Eq. (10) to accurately represent the cyclic plastic strain response. The effective RSS on slip system α is

$$\tau_{\text{eff}}^\alpha = \tau^\alpha - \sum_i B_i^\alpha \quad (11)$$

The plastic shearing rate $\dot{\gamma}^\alpha$ on slip system α is

$$\dot{\gamma}^\alpha = \dot{\gamma}_0 \left| \frac{\tau_{\text{eff}}^\alpha}{s^\alpha} \right|^m \text{sgn}(\tau_{\text{eff}}^\alpha) \quad (12)$$

where $\dot{\gamma}_0$ is the reference shearing rate, m is the slip rate sensitivity, and s^α is the non-directional slip resistance on slip system α . As m is small for coarse-grained stainless steel, the simulated viscoplastic response approaches its rate-independent counterpart. The slip resistance s^α , with an initial value s_0^α , evolves according to

$$\dot{s}^\alpha = \sum_\beta h^{\alpha\beta} |\dot{\gamma}^\alpha| \quad (13)$$

The matrix of the strain hardening rate is

$$[h^{\alpha\beta}]_{12 \times 12} = \begin{cases} h^\beta & \text{if } \alpha = \beta \\ qh^\beta & \text{if } \alpha \neq \beta \end{cases} \quad (14)$$

where q is the latent hardening coefficient taken as 1.4 (Asaro and Needleman, 1985); and h^β is the single slip hardening rate, which is taken as (Kalidindi et al., 1992)

$$h^\beta = h_0 \left\{ 1 - \frac{s^\beta}{s_s} \right\}^{a_0} \quad (15)$$

where h_0 is the initial hardening rate, a_0 is the hardening exponent and s_s is the saturated non-directional slip resistance. These hardening parameters are taken to be identical for all 12 $\{111\}\langle 101 \rangle$ slip systems. The CP model is implemented by writing an Abaqus/Explicit user subroutine VUMAT (ABAQUS/Explicit, 2009).

2.3. Application of JP and CP models to 316L stainless steel

In this work, both the cyclic JP and CP models are applied to polycrystalline 316L stainless steel. The cyclic tension and compression data are taken from the experimental measurements (Pham et al., 2013) at a strain rate of 10^{-3} s^{-1} and a temperature of 20 °C, with a completely reversed strain amplitude of $\pm 0.7\%$. For the JPFE simulation of cyclic tension and compression, strain-controlled load cycles are applied to a single linear brick element to fit the cyclic JP parameters of polycrystalline 316L. For the corresponding CPFEE simulation, the same cyclic loading condition is applied to a polycrystalline cube consisting of $5 \times 5 \times 5$ brick elements, with each representing a grain with a random orientation, thereby fitting the cyclic JP parameters of polycrystalline 316L. The fitting parameters for the JP and CP models are listed in Table 1 and Table 2, respectively. Fig. 1 shows that after a few initial cycles, the simulated cyclic stress-strain curves of polycrystalline 316L by the two models closely match the experimentally measured stable hysteresis loop (Pham et al., 2013), despite small differences between their initial tensile loading branches. Such differences are not of significant concern, as our primary objective is to model stable cyclic crack growth, a process primarily governed by the stable hysteresis loop rather than strongly impacted by the initial tensile loading branches in JP and CP models. It is also seen from Fig. 1 that the pronounced Bauschinger effect in 316L is evident by the occurrence of early reverse yielding in unloading branches.

2.4. Crack models

We study a semi-infinite crack embedded in a polycrystal subjected to a far-field load of mode I stress intensity factor K . Considering the structural and load symmetry with respect to the crack plane, we represent the cracked polycrystalline system by a semi-circular domain, as depicted in Fig. 2a. We employ two models to represent this semi-circular domain. In the first model, this domain is treated

Table 1
Parameters for 316L stainless steel in the cyclic JP model.

E	ν	G	σ_{y0}	Q_∞	b
193 GPa	0.27	76 GPa	55 MPa	80 MPa	100
C_1	D_1	C_2	D_2	C_3	D_3
135 GPa	1000	203 GPa	11,000	5 GPa	5

Table 2
Parameters for 316L stainless steel in the cyclic CP model.

C_{11}	C_{12}	C_{44}	$\dot{\gamma}_0$	m	s_0^{σ}	s_s
204.6 GPa	137.7 GPa	126.2 GPa	1.0	0.02	50 MPa	70 MPa
h_0	a_0	q	\tilde{C}_1	\tilde{D}_1	\tilde{C}_2	\tilde{D}_2
1000 MPa	4	1.4	60 GPa	1000	4 GPa	100

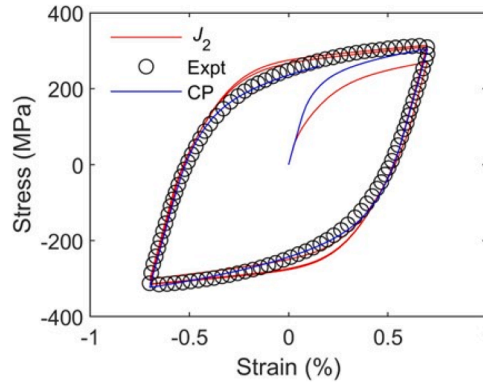


Fig. 1. Comparison of uniaxial stress-strain hysteresis loops between experimental measurements (Pham et al., 2013) and cyclic JPFE and CPFE simulations for polycrystalline 316L stainless steel under strain-controlled cyclic loading.

as a homogenized medium without explicit consideration of its constituent grains, as illustrated in Fig. 2b, and the plastic response of the domain is represented by the cyclic JP constitutive model in Section 2.1. In the second model, the entire domain is treated as a single crystal, which is a simplified representation of a polycrystalline domain, as also illustrated in Fig. 2b. The cyclic behavior of the single crystal domain is represented by the cyclic CP constitutive model in Section 2.2.

The single crystal domain in the second model serves two purposes. First, it is used to study the crack tip deformation fields in single crystals with different orientations relative to the crack plane under monotonic loading, in order to understand the corresponding CPFE simulation results through comparison with theoretical and experimental findings in previous studies. Second, it serves as a simplified model to study the cyclic plastic response at the crack tip of polycrystals under cyclic loading. When an applied cyclic load is low, the cyclic plastic zone is primarily limited within the crack tip grain (highlighted in red in Fig. 2a), while other neighboring grains remain dominantly elastic. When the elastically deformed grains surrounding the crack tip grain are assumed to have the same orientation as the crack tip grain, the entire semi-circular domain is simplified as a single crystal. Essentially, we neglect the non-uniform deformation caused by the elastic anisotropy of grains with different orientations near the crack tip. This simplified model yields somewhat different crack tip deformation fields compared to those in a polycrystalline sample. However, our FE results indicate that this difference has a limited influence on simulated crack tip Mises stresses between the JP and CP models under both monotonic and cyclic loading, supporting the use of the simplified model. Nonetheless, it is necessary to further determine the effective K load on the simplified single crystal model based on the K load applied to the corresponding polycrystal in the future.

Fig. 3a shows the FE model of a semi-circular disk with a radius R , including its mesh, following the setup used by Sofronis and McMeeking (1989). Since this work is focused on plane strain deformation, it is possible to employ a 2D half disk. However, we choose to use a 3D half disk with a small thickness. The reason for this choice is our intention to develop a full 3D cyclic CP model of fatigue crack growth in future research. Using a quasi-3D setup in this study can facilitate its future extension to a complete 3D model. Within

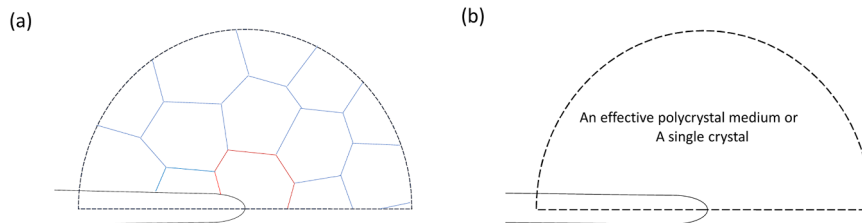


Fig. 2. Schematic illustration of the crack models used in this study. (a) A semi-infinite crack embedded in a polycrystal subjected to a mode I K load. Due to structural and load symmetry, the cracked system is represented by a semi-circular domain. (b) For the crack models used in this study, the semi-circular domain in (a) is either treated as a homogenized medium without explicit consideration of its constituent grains or as a single crystal throughout the entire domain.

the semi-circular disk, a notched crack tip is placed at the center of the bottom section. We impose symmetry boundary conditions on the bottom of the domain to the right of the crack tip, while the bottom of the domain to the left of the crack tip is specified as traction free. The outer semi-circular boundary of the disk is subjected to applied displacements (Deka and Jonnalagadda, 2017; Patil et al., 2008b; Zirkle and McDowell, 2022) based on the Williams solution for a linear elastic mode I crack under plane strain conditions (Williams, 1957), as given by

$$u_1 = \left(\frac{r}{2\pi}\right)^{1/2} \frac{1+\nu}{E} K \cos\left(\frac{\theta}{2}\right) \left(\kappa - 1 + 2\sin^2\left(\frac{\theta}{2}\right)\right) \quad (16)$$

$$u_2 = \left(\frac{r}{2\pi}\right)^{1/2} \frac{1+\nu}{E} K \sin\left(\frac{\theta}{2}\right) \left(\kappa + 1 - 2\cos^2\left(\frac{\theta}{2}\right)\right) \quad (17)$$

where (r, θ) are the polar coordinates in Fig. 3a; u_1 and u_2 are the displacements in the x_1 and x_2 directions, respectively; E is Young's modulus, ν is Poisson's ratio, and $\kappa = 3 - 4\nu$ for the plane strain condition.

We employ a sufficiently large simulation domain to ensure the applicability of the Williams solution at the outer boundary. For the semi-circular disk model in Fig. 3a, we set its outer radius as $R = 2000r_0$, where r_0 is the notch radius. We take $r_0 = 5 \mu\text{m}$, such that $R = 10 \text{ mm}$. Fig. 3a also shows the graded FE mesh, with refinement near the crack tip and gradual coarsening when moving away from the crack tip. Fig. 3b provides a close-up view of the graded mesh within a small radius of $50 \mu\text{m}$ near the crack tip. With a small thickness of $0.2 \mu\text{m}$ for the semi-circular disk, we use 3D linear elements (C3D8) with one element through the thickness of the disk. The in-plane element size is approximately $1 \mu\text{m}$ near the crack tip. The displacement boundary conditions in Eqs. (16) and (17) are imposed through a Abaqus/Explicit user subroutine VDISP (ABAQUS/Explicit, 2009). We apply a constant K loading rate of $0.67 \text{ MPa}\sqrt{\text{m}}/\text{s}$, which is typical of previous crack simulations for metal alloys (Sofronis and McMeeking, 1989). The values of E and ν used in Eqs. (16) and (17) correspond to those of polycrystalline 316L stainless steel, as listed in Table 1.

2.5. Crack orientations and active slip systems

To investigate crack tip fields in the semi-circular domain represented by a single crystal, we consider two symmetric crack orientations. Our simulated crack tip fields are compared with those of earlier studies (Saeedvafa and Rice, 1989). Fig. 4 illustrates the crack orientations and the active slip systems in fcc single crystals under plane strain conditions. For the first crack orientation, the crack plane is (010), and the crack front aligns with the face diagonal $[\bar{1}01]$ direction, such that the crack propagates along the face diagonal [101] direction. For the second crack orientation, the crack plane is (101), and the crack front aligns with the $[\bar{1}01]$ direction, such that the crack propagates along the [010] direction. Hereafter, we refer to the crack with the first orientation as the (010)[101] crack and the one with the second orientation as the (101)[010] crack. These two crack orientations are frequently observed in experiments (Garrett and Knott, 1975; Neumann, 1974a,b) and are commonly studied (Crone and Shield, 2001; Crone et al., 2004, 2003; Cuitino and Ortiz, 1996, 1993; Drugan, 2001; Flouriot et al., 2003a; Forest et al., 2001; Karamitros et al., 2022; Mohan et al., 1992; Patil et al., 2009, 2008a; Rice et al., 1990; Rice, 1987; Saeedvafa and Rice, 1989; Sakaguchi et al., 2019; Shield, 1996; Shield and Kim, 1994; Zirkle and McDowell, 2022). Because the crystal structure is symmetric with respect to the crack plane and crack growth direction, our modeling focuses only on the upper half crystal above the crack plane (Fig. 2).

For the (010)[101] crack under mode I loading, three out of four active $\{111\}$ slip planes, including (111), $(1\bar{1}1)$ and $(\bar{1}11)$, are shown by shaded triangles in a reference fcc single crystal cube (Fig. 4a). The fourth active slip plane $(1\bar{1}\bar{1})$ is symmetric with $(\bar{1}11)$ about the $(\bar{1}01)$ plane and is not directly visible in Fig. 4a. The slip directions are generally along diagonals $\langle 110 \rangle$ of these $\{111\}$ slip planes, i.e., the sides of the shaded triangles. Note that plane strain deformation dictates slip on six $\{111\}\langle 110 \rangle$ slip systems, which belong to three types of active slip systems. Specifically, for the edge-on (111) slip plane, shear parallel to this slip plane should involve

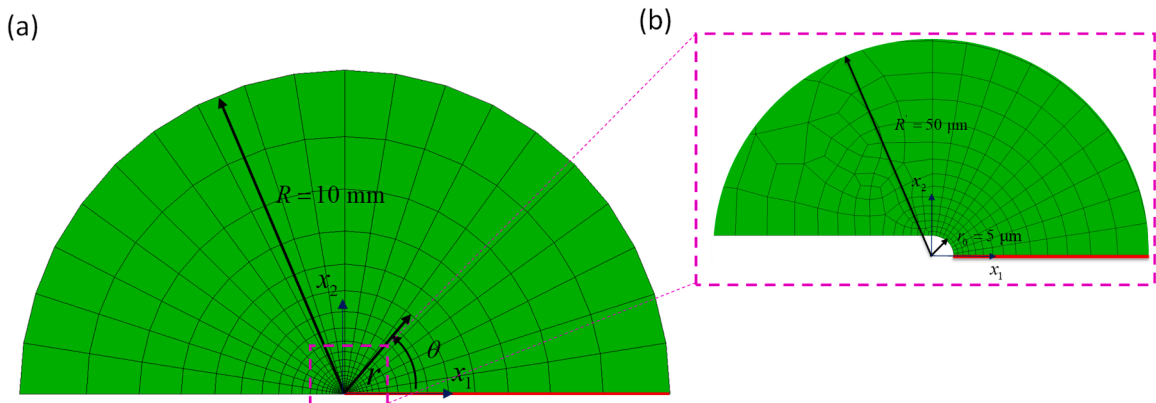


Fig. 3. Geometry and FE mesh of a semi-circular crack model. (a) Overview of the crack model. (b) Close-up view of the near-tip region.

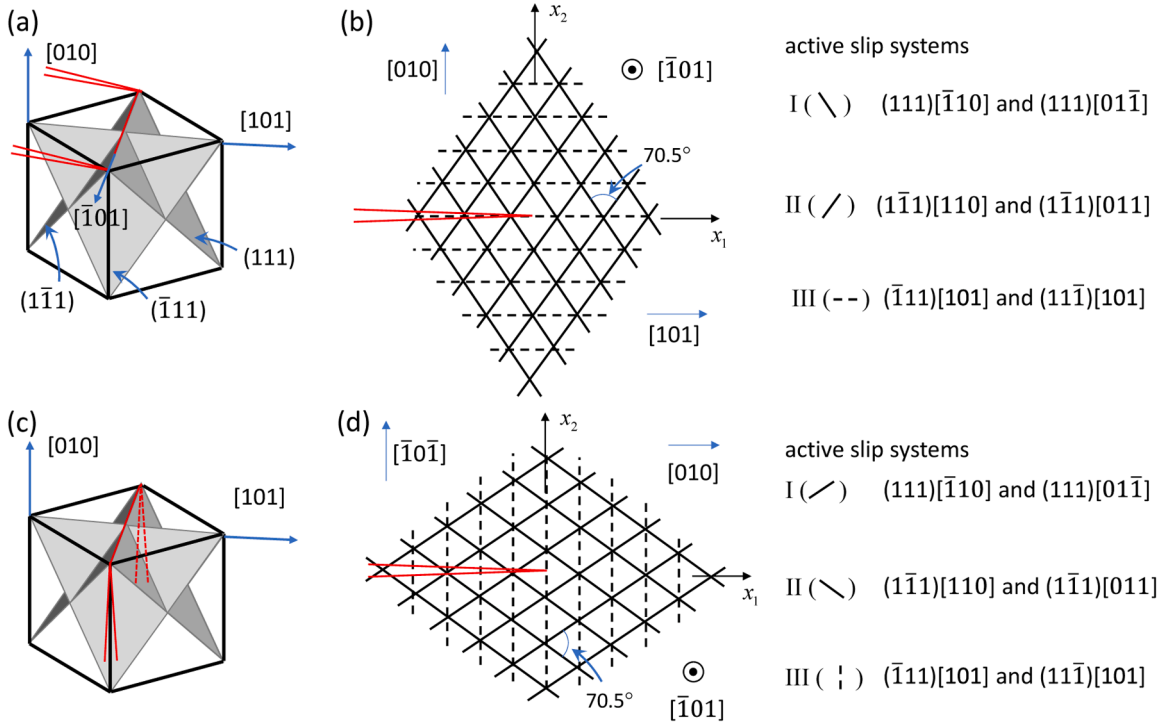


Fig. 4. Crack orientations and activated slip systems during plane strain deformation. (a) A (010)[101] crack is illustrated with an fcc crystal cube. Three out of four active {111} slip planes compatible with plane strain conditions are shown by shaded triangles. (b) Slip traces resulting from the intersection of three types of active slip systems (denoted as I, II and III) with the $x_1 - x_2$ plane. (c) Same as (a) except for a (101)[010] crack. (d) Same as (b) except for a (101)[010] crack.

simultaneous and equal amounts of slip along the $[1\bar{1}0]$ and $[01\bar{1}]$ directions that cancel their out-of-plane slip components, resulting in effective, composite slip along the $[\bar{1}2\bar{1}]$ direction on the $(\bar{1}01)$ plane. Hence, the effective $(111)[\bar{1}2\bar{1}]$ slip results from a combination of slips on $(111)[\bar{1}10]$ and $(111)[01\bar{1}]$, which are referred to as type I slip systems. The same consideration is applied to another edge-on $(\bar{1}\bar{1}1)$ slip plane. Correspondingly, the effective $(\bar{1}\bar{1}1)[121]$ slip results from a combination of slips on $(\bar{1}\bar{1}1)[110]$ and $(\bar{1}\bar{1}1)[011]$, referred to as type II slip systems. Traces of (111) and $(\bar{1}\bar{1}1)$ slip planes intersecting the $x_1 - x_2$ plane are indicated as solid lines in Fig. 4b. In addition, plane strain deformation dictates simultaneous and equal amounts of slip on $(\bar{1}\bar{1}1)$ and $(11\bar{1})$ slip planes along the same in-plane $[101]$ direction. Traces of $(\bar{1}\bar{1}1)$ and $(11\bar{1})$ slip planes intersecting the $x_1 - x_2$ plane are shown as dashed lines in Fig. 4b. Correspondingly, the effective $(010)[101]$ slip results from a combination of slips on $(11\bar{1})[101]$ and $(\bar{1}\bar{1}1)[101]$, referred to as type III slip systems. The three types of active slip systems are listed in Fig. 4b. A similar analysis of active slip systems can be given for the $(101)[010]$ crack under mode I loading and plane strain conditions. As shown in Fig. 4c and d, the resulting slip traces in the $x_1 - x_2$ plane are equivalent to those Fig. 4a and b, but differ by an in-plane 90° rotation, as the crack plane is aligned with the x_1 axis. The corresponding three types of active slip systems are listed in Fig. 4d.

2.6. Fatigue crack growth model

Based on the FE results of crack tip fields, we employ a critical accumulated plastic work criterion to determine the fatigue crack growth rate. Recently, Hosseini et al. (Hosseini et al., 2018) developed an FE methodology for evaluating fatigue crack growth rates in ductile materials based on accumulated plastic work. Their approach represented material responses by the Chaboche cyclic JP model without explicit consideration of grain-level plastic deformation. Crack advancement was simulated by nodal release when the accumulated plastic work density in the crack tip element reached a critical threshold. Hence, the size of each increment in crack growth corresponds to that of the crack tip element. This element-based growth model is typically sensitive to mesh size at the crack tip. In another recent study, Karamitros et al. (Karamitros et al., 2022) adopted a critical stored energy density criterion to evaluate fatigue crack growth rates based on the eXtended FE method (XFEM) simulation of crack propagation. They used a nonlocal method to account for crack tip plastic strain gradients, thus regularizing the solution and reducing sensitivity to mesh size. Here we utilize a critical accumulated plastic work criterion as a surrogate driving force parameter to model fatigue crack growth rates based on stationary cracks, without explicit modeling of crack growth processes (Lu et al., 2023; Zhou et al., 2015). To mitigate mesh sensitivity, we assume that once the accumulated plastic work density, averaged over the cyclic plastic zone, reaches a critical threshold, the crack will advance by an amount equal to the cyclic plastic zone size. This criterion, insensitive to mesh size at the crack tip, is therefore

employed to determine fatigue crack growth rates for both the cyclic JPFE and CPFE simulations of stationary cracks.

For our FE crack simulations using the cyclic JP model, the accumulated plastic work W_p is calculated as

$$W_p = \int_t \int_A \boldsymbol{\sigma} : \dot{\boldsymbol{\epsilon}}^p dAdt \quad (18)$$

where A is the area of the cyclic plastic zone encompassing finite elements with non-vanishing $\dot{\boldsymbol{\epsilon}}^p$, and t is the time. The value of W_p is taken from the ABAQUS history output for the plastic work of the entire system, which corresponds to the value of W_p in the cyclic plastic zone.

For our FE crack simulations using the cyclic CP model, the accumulated plastic work W_p is calculated as

$$W_p = \sum_\alpha \int_t \int_A \tau^\alpha \dot{\gamma}^\alpha dAdt \quad (19)$$

The calculation of W_p in Eq. (19) is implemented in the VUMAT. The plastic work density per unit area in the cyclic plastic zone and per cycle \bar{w}_p is obtained by

$$\bar{w}_p = \frac{W_p/A}{N} = \frac{w_p}{N} \quad (20)$$

where w_p is the plastic work density accumulated in N cycles. Note that W_p usually exhibits a nonlinear increase with N in the first few loading cycles. Afterwards, it approaches a steady, constant value dW_p/dN as the cyclic stress-strain response stabilizes within the cyclic plastic zone. Hence, we determine \bar{w}_p from the stabilized response with a constant dW_p/dN , which is used to evaluate the fatigue crack growth rate.

To relate the crack growth rate to the applied range of stress intensity factor ΔK , the Paris law is used

$$\frac{da}{dN} = C\Delta K^m \quad (21)$$

where a is the crack length, C and m are material parameters that are usually determined by fitting the experimental or modeling data of da/dN vs. ΔK . In our model, the crack growth rate is calculated as

$$\frac{da}{dN} = \frac{s}{N^c} \quad (22)$$

where s is the size of the stabilized cyclic plastic zone, N^c is the number of cycles required to reach the critical plastic work density w_p^c , and it is given by

$$N^c = \frac{w_p^c}{\bar{w}_p} \quad (23)$$

The area of the cyclic plastic zone A is estimated as $A \approx s^2$, which is then combined with Eqs. (20), (22) and (23) to calculate the crack growth rate

$$\frac{da}{dN} = \frac{W_p/N}{s w_p^c} \quad (24)$$

For a given ΔK , W_p and s are calculated from the corresponding FE simulation involving N cycles with the stabilized response of dW_p/dN . Clearly, this approach appeals to correlation of the fatigue crack growth rate with the nonlocal cyclic plastic work W_p at the crack tip, akin to a ΔJ integral approach (McDowell, 1996; McDowell and Berard, 1992). For a specified w_p^c value, we use Eq. (24) to determine da/dN vs. ΔK for all cases. Once we obtain pairs of data for da/dN vs. ΔK , we can rewrite the Paris law of Eq. (21) as $\ln(da/dN) = \ln C + m \ln \Delta K$ and adjust the value of w_p^c to match the simulated C value with the experimental C value. It is noted that a change of w_p^c only affects C , not m . Thus, the simulated Paris exponent m , corresponding to use of the cyclic plastic work as a surrogate driving force parameter, is independent of the fitted value of w_p^c . It is also noted that other surrogate measures of fatigue crack driving force could be introduced and computed following a similar methodology. The resulting value of m for some measures will more accurately reflect connections to the irreversible cyclic crack tip displacement range than others in comparison with experiments, as discussed later. For purposes of this work, the choice of W_p suffices to provide a surrogate measure of fatigue crack driving force.

3. Results and discussion

3.1. Crack tip fields under cyclic loading from JPFE simulations

Cyclic JPFE simulations are performed to investigate crack tip fields in 316L stainless steel under cyclic loading. The cyclic loading profile, in terms of applied K , is depicted in Fig. 5a, where the maximum and minimum K values are $K_{\max} = 15 \text{ MPa}\sqrt{\text{m}}$ and $K_{\min} = 0$,

respectively. The corresponding R ratio K_{\min}/K_{\max} is zero and the K range $\Delta K = K_{\max} - K_{\min}$ is $15 \text{ MPa}\sqrt{\text{m}}$. Under cyclic loading, it is in general necessary to consider crack closure due to contact between crack faces in determining the effective stress intensity factor (Suresh, 1998). Although crack closure has been observed in numerical studies involving initially sharp cracks (Hosseini et al., 2018), it does not occur in our simulations owing to the initially blunted crack tip. Since the cyclic JP model achieves an essentially stable stress-strain hysteresis loop by the third load cycle (Fig. 1), cyclic crack simulations are performed for up to 10 cycles to determine the steady rates of dW_p/dN used in modeling fatigue crack growth rates.

Fig. 5b–d show the Mises stress contours and the evolution of the plastic zone under cyclic loading, with the corresponding K load indicated in Fig. 5a. Given the variation of yield stress during initial cycling (Fig. 1), we characterize the plastic zone using a nominal yield stress of 150 MPa for 316L stainless steel. Fig. 5b displays the Mises stress contour near the crack tip at $K_{\max} = 15 \text{ MPa}\sqrt{\text{m}}$, with the grey region representing the plastic zone. Fig. 5c presents the Mises stress contour at $K_{\min} = 0$, with the grey region representing the plastic zone undergoing reverse yielding. As shown in Fig. 1, 316L stainless steel exhibits a strong Bauschinger effect, resulting in pronounced asymmetry of response in forward and reverse yield stresses. This effect leads to an increase in the size of the plastic zone undergoing reverse yielding at $K_{\min} = 0$ compared to the model without the Bauschinger effect. During subsequent cycling, the differences between the plastic zones at K_{\max} and K_{\min} within each cycle reduce with increasing cycle number, as the stress-strain hysteresis loop stabilizes quickly (Fig. 1). As evident from Fig. 5d and e, the plastic zones at K_{\max} and K_{\min} in the 8th cycle exhibit much closer shapes and sizes. Any remaining small differences can primarily be attributed to the positive mean of K_{\max} and K_{\min} .

3.2. Crack tip fields under monotonic loading from CPFE simulations

The cyclic CP model is used to investigate crack tip fields under both monotonic and cyclic loading. We perform a detailed analysis of crack tip fields in the semi-circular single crystal domain (depicted in Fig. 2b) in the first half of the load cycle, which corresponds to the crack response under monotonic loading. We consider two crack orientations and compare them with previous asymptotic solutions, FE simulations, and experimental observations under monotonic loading conditions (Crone and Shield, 2001; Crone et al., 2004, 2003; Saeedvafa and Rice, 1989; Shield, 1996; Shield and Kim, 1994).

Fig. 6 shows the Mises stress contours for the (010)[101] and (101)[010] cracks at $K_{\max} = 15 \text{ MPa}\sqrt{\text{m}}$. As in Fig. 5, we use a nominal yield stress of 150 MPa to characterize the plastic zone. It is seen from Fig. 6a and b that the shape and size of the plastic zone are markedly different for the two crack orientations, which can be attributed to the elastic and plastic anisotropies of single crystal stainless steel. Furthermore, their plastic zone sizes are larger than that from the cyclic JPFE simulation under the same load (Fig. 5b). This difference can primarily be attributed to varying yield stresses in the first load cycle between the cyclic CP and JP models (Fig. 1). However, the differences in cyclic plastic zone sizes are reduced as the stress-strain hysteresis loops stabilize and converge between the two cyclic plasticity models (as discussed later).

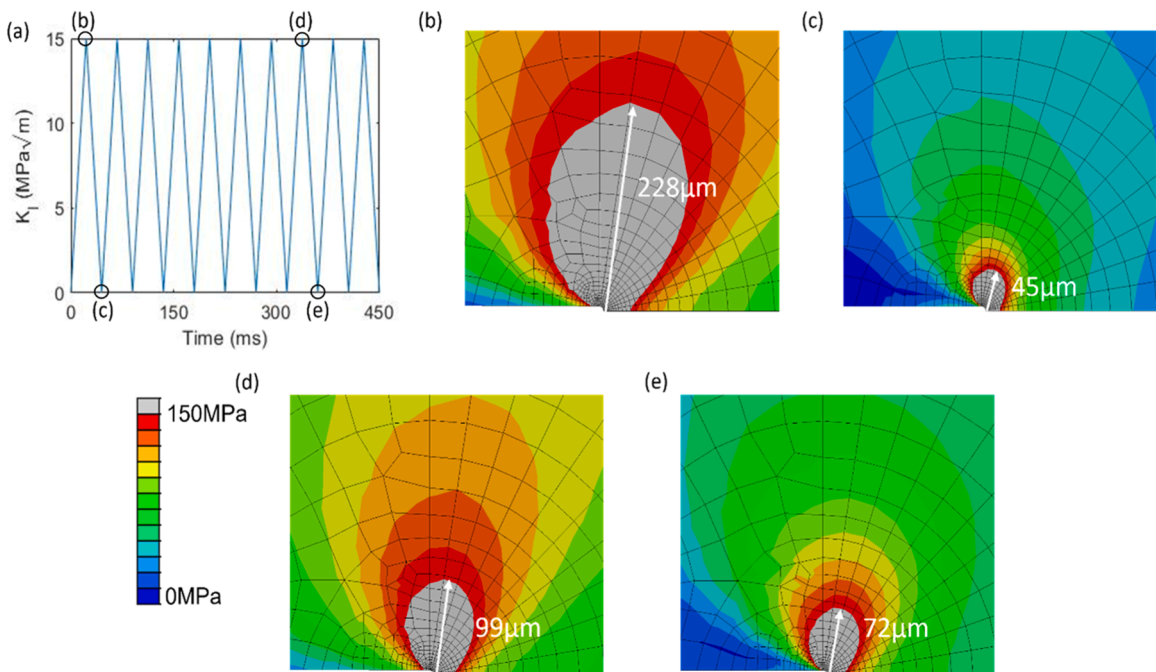


Fig. 5. Crack tip Mises stress contours and plastic zones under cyclic loading from JPFE simulations. (a) Schematic of loading cycles with $\Delta K=15 \text{ MPa}\sqrt{\text{m}}$. (b–e) Mises stress contours showing cyclic plastic zone sizes at different load cycles marked in (a). A nominal yield stress of 150 MPa is used as the upper limit of the stress contour, such that the grey region represents the plastic zone where the Mises stress exceeds the nominal yield stress.

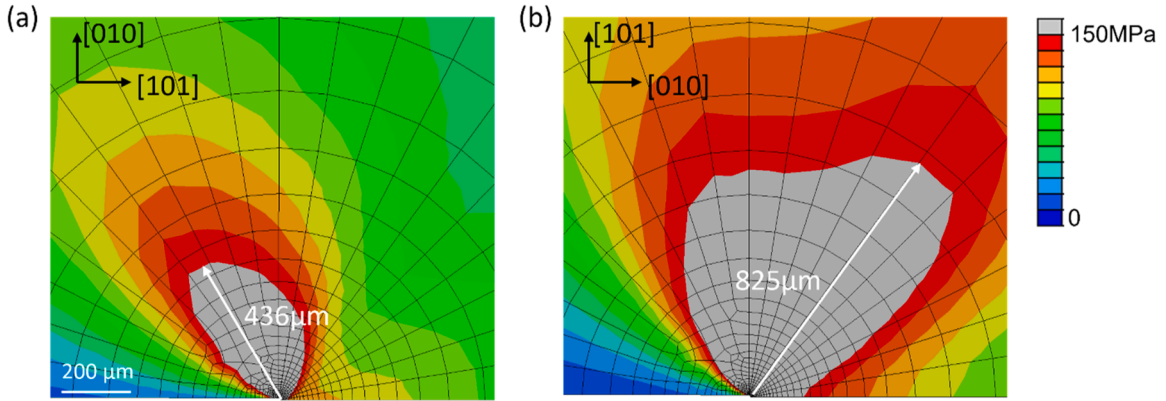


Fig. 6. Crack tip Mises stress contours and plastic zones in the first half load cycle (corresponding to monotonic loading) from CPFE simulations. (a) (010)[101] crack and (b) (101)[010] crack at $K = 15 \text{ MPa}\sqrt{\text{m}}$. A nominal yield stress of 150 MPa is used as the upper limit of the stress contour, such that the grey region represents the plastic zone where the Mises stress exceeds the nominal yield stress.

Fig. 7 shows the slip strain contours for the three types of active slip systems compatible with plane strain deformation for the two crack orientations. In each contour plot, the white solid or dashed line represent the orientation of slip traces of the corresponding active slip plane intersecting the $x_1 - x_2$ plane, as depicted in Fig. 4. For the (010)[101] crack, the large backward-leaning lobe in Fig. 7a1, corresponding to the light blue region enclosed by a constant strain contour of 0.00017, is associated with type I slip systems of $(111)\bar{1}10$ and $(111)01\bar{1}$; the forward-leaning lobe in Fig. 7a2 is associated with type II slip systems of $(\bar{1}\bar{1}1)110$ and $(\bar{1}\bar{1}1)011$; and the slightly backward-leaning lobe in Fig. 7a3 is associated with type III slip systems of $(\bar{1}11)101$ and $(1\bar{1}1)101$. In contrast, for the (101)[010] crack, the large forward-leaning lobe in Fig. 7b1 is associated with type I slip systems of $(111)\bar{1}10$ and $(111)01\bar{1}$, and it contrasts with the large backward-leaning one in Fig. 7a1. This change in leaning orientation arises because for the (101)[010] and (010)[101] cracks, the same type of slip systems are oriented differently relative to the horizontal crack plane, with their slip planes differing by an in-plane 90° rotation. In addition, for the (101)[010] crack, the large forward-leaning lobe in Fig. 7b2 and the slightly backward-leaning lobe in Fig. 7b3 are associated with type II and III slip systems, respectively; and they do not change leaning orientations compared to Fig. 7a2 and a3 for the (010)[101] crack, respectively, despite the orientation of the corresponding slip planes differ by an in-plane 90° rotation for the two crack orientations.

The above results contrast with the asymptotic solutions derived from small strain formulation, which yield identical crack tip fields for the two crack orientations (Saeedvafa and Rice, 1989). These asymptotic solutions are supported by an FE study employing small strain formulation (Rice et al., 1990), which gives identical effective shear strain distributions for the (010)[101] and (101)[010] cracks. This is because Eq. (8) can be expressed as $\mathbf{S}_0^\alpha = \frac{1}{2} (\mathbf{m}_0^\alpha \otimes \mathbf{n}_0^\alpha + \mathbf{n}_0^\alpha \otimes \mathbf{m}_0^\alpha)$ where the slip direction \mathbf{m}_0^α and the slip plane normal direction \mathbf{n}_0^α are interchangeable for small strain analysis. Consequently, crack tip fields for crack orientations that differ by an in-plane 90° rotation are identical. In small strain analysis, the regular shear parallel to the long axis of the elongated shear region and the kink-like shear perpendicular to the long axis are indistinguishable because \mathbf{m}_0^α and \mathbf{n}_0^α are interchangeable. However, when finite deformation is accounted for, the tendency to regular and kink-like shear differs due to a geometrical softening or hardening effect induced by finite lattice rotation. In fact, our finite deformation CPFE simulations not only give different crack tip fields for the two crack orientations, but also distinguish regular and kink-like shear responses. For example, the forward-leaning lobe in Fig. 7a2 exhibits elongation along the trace of type II slip systems, indicating a regular shear response. In contrast, the forward-leaning lobe in Fig. 7b2 is elongated along the direction perpendicular to the trace of type II slip systems, indicating a kink-like shear response. Previous studies have recognized different crack tip fields from finite deformation as opposed to small strain analysis. For example, Mohan et al. (Mohan et al., 1992) obtained different crack tip fields from finite deformation CPFE simulations for (010)[101] and (101)[010] cracks, but regained small strain solutions (Saeedvafa and Rice, 1989) by removing finite deformation kinematics from their model. Our slip strain distributions in Fig. 7 are consistent with the corresponding results by Mohan et al. (Mohan et al., 1992).

Whereas the aforementioned asymptotic solutions are obtained based on small strain analysis, they can still be used to approximately determine the angular sector distribution and associated active slip systems close to the crack tip. These asymptotic solutions are known to be affected by strain hardening behavior. Employing a power-law isotropic hardening constitutive relation, the asymptotic solutions (Saeedvafa and Rice, 1989) showed more complex stress distributions and sectors with varying active slip systems compared to their perfectly plastic counterparts (Rice, 1987). As discussed in Section 2.2, we adopt a power-law hardening relation in the cyclic CP model. We calculate the angular distribution of RSS on different slip systems and then determine the sector distributions and associated active slip systems, as shown in Fig. 8. More specifically, the RSS τ^α on slip system α is calculated by

$$\tau^\alpha = m_i^\alpha \sigma_{ij} n_j^\alpha \quad (25)$$

where σ_{ij} is the Cauchy stress, m_i^α and n_j^α are the current configuration vectors in the slip direction and slip plane normal direction of slip system α , respectively. A slip system is deemed activated when the magnitude of τ^α reaches a critical value. From CPFE simulations,

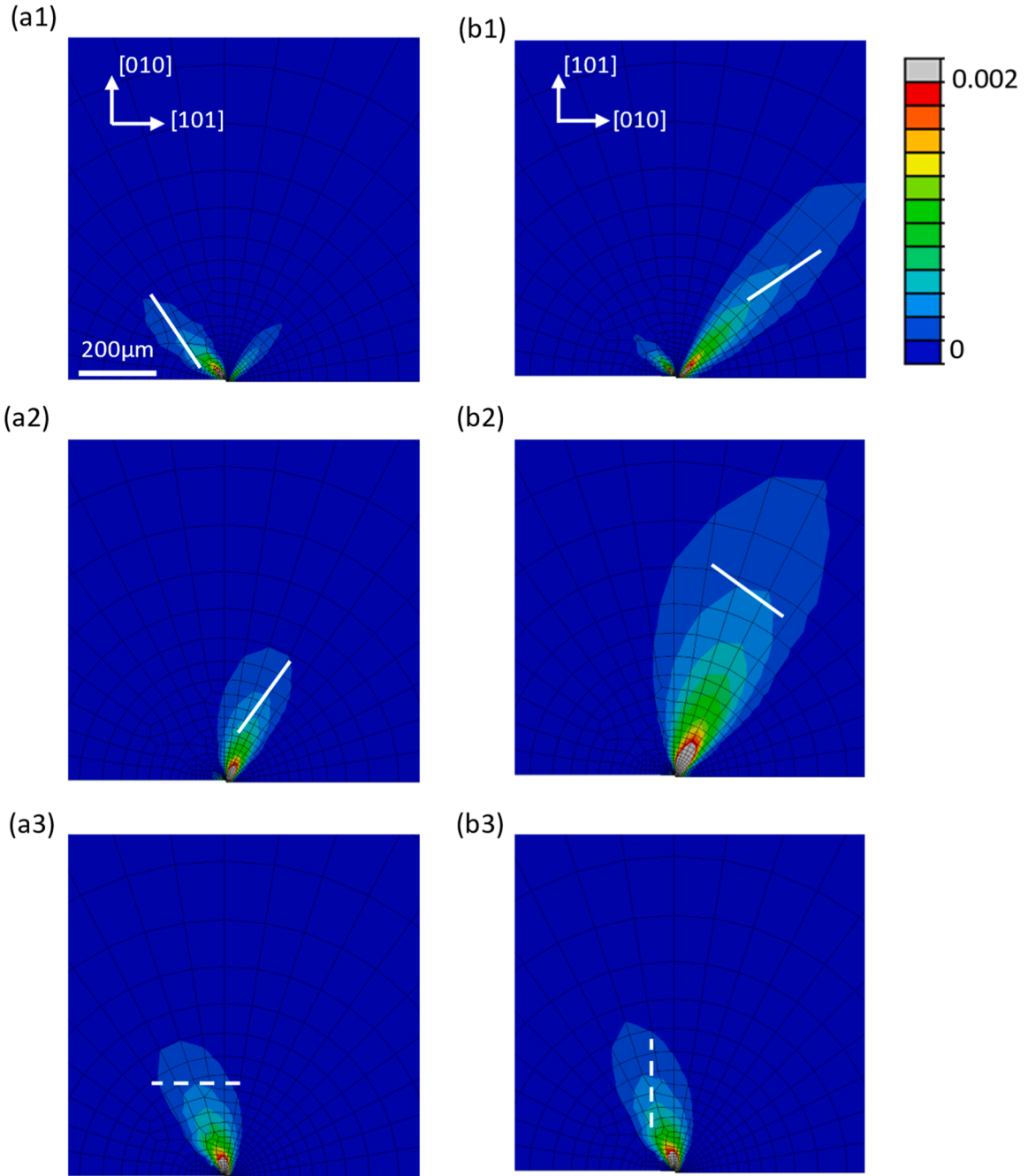


Fig. 7. Distributions of slip strain on three types of active slip systems for (010)[101] and (101)[010] cracks at $K = 15 \text{ MPa}\sqrt{\text{m}}$. For the (010)[101] crack, contours of slip strain are shown for (a1) type I slip systems of $(111)\bar{1}10$ and $(111)01\bar{1}$, (a2) type II slip systems of $(\bar{1}\bar{1}1)110$ and $(\bar{1}\bar{1}1)011$, (a3) type III slip systems of $(11\bar{1})101$ and $(\bar{1}\bar{1}1)101$. For the (101)[010] crack, contours of slip strain are shown for (b1) type I slip systems of $(111)\bar{1}10$ and $(111)01\bar{1}$, (b2) type II slip systems of $(\bar{1}\bar{1}1)110$ and $(\bar{1}\bar{1}1)011$, (b3) type III slip systems of $(\bar{1}\bar{1}1)101$ and $(11\bar{1})101$. White solid and dashed lines indicate traces of the corresponding active slip planes intersecting the $x_1 - x_2$ plane.

we extract σ_{ij} at a radial distance $r = 70 \mu\text{m}$ ($14r_0$) close to the crack tip and calculate the angular distribution of τ^a on each type of active slip system, as shown in Fig. 8a and b for the two crack orientations, respectively. Recall that the angle θ is defined in Fig. 2a, such that $\theta = 0^\circ$ corresponds to the positive x_1 axis ahead of the crack tip and 180° corresponds to the negative x_1 axis behind the crack tip. The horizontal dashed lines in Fig. 8a and b indicate the critical magnitude of τ^a for activation of each slip system, set at 60 MPa, corresponding to the average of initial and saturated slip resistances. Based on Fig. 8a and b, the arrangement of seven plastic sectors together with the active slip systems in each sector are determined for the two crack orientations, as shown in Fig. 8c and d,

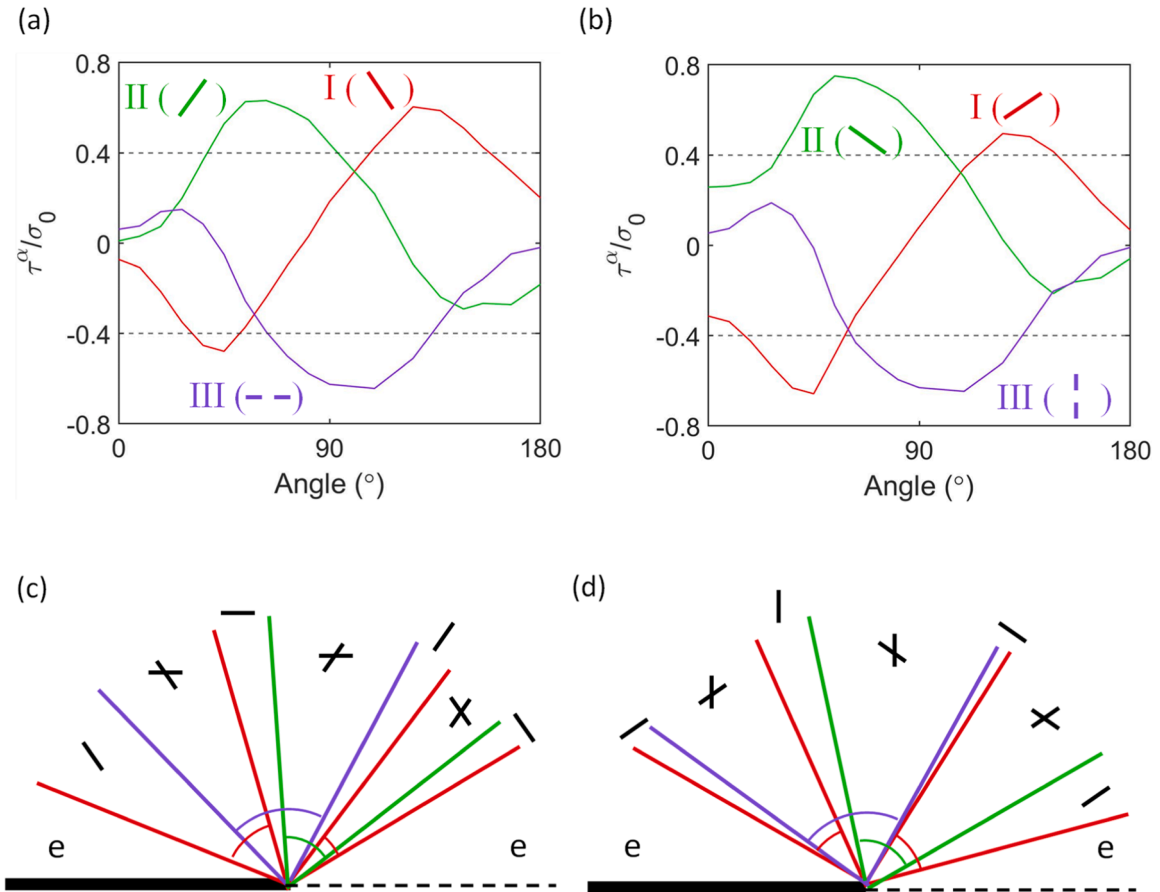


Fig. 8. Resolved shear stress and the arrangement of angular sectors of different active slip systems along an angular path with the radial distance $r = 70 \mu\text{m}$ for (010)[101] and (101)[010] cracks at $K = 15 \text{ MPa}\sqrt{\text{m}}$. (a-b) Angular distributions of resolved shear stress on the three types of active slip systems for the (010)[101] crack and (101)[010] crack, respectively. (c-d) Sketch of the sector boundaries for the (010)[101] crack and (101)[010] crack, respectively. Short black segments indicate slip plane orientations of the active single or double slip in each sector.

respectively. It is seen that the active slip systems in the seven plastic sectors exhibit a pattern of alternating single slip and double slip with increasing θ . This pattern emerges because the active slip systems in plastic sectors with increasing θ are governed by traversing the yield surface of a single crystal under plane strain deformation, which features connected straight segments and vertices corresponding to single and double slips, respectively (Saeedvafa and Rice, 1989).

We note that the plastic sector results for the two orthogonal crack orientations are not exactly identical, due to the finite deformation formulation of the CP model used. Additionally, for the (010)[101] crack, the arrangement of the seven plastic sectors, along with the active slip systems in each sector in Fig. 8c, is qualitatively consistent with the asymptotic solution of plastic sectors (Saeedvafa and Rice, 1989), which assumes that the entire near-tip field responds plastically. In contrast, elastic sectors labelled as “e” (i.e., angular regions without active slip systems) are present ahead of and behind the crack tip in both Fig. 8c and d, whereas they are absent in the asymptotic solutions. This difference could be attributed to the fact that the analysis of plastic sectors from CPFE results is obtained at a small yet finite radial distance $r = 70 \mu\text{m}$ from the crack tip, while the asymptotic solution represents the limit as r approaches zero. We further note that the sector boundaries in Fig. 8c and d are depicted as straight lines, representing the angular distributions of plastic sectors at the radial distance around $r = 70 \mu\text{m}$ near the crack tip. As the angular stress distributions vary with r , curved sector boundaries emerge, as indicated by sector analyses conducted at varying radial distances from the crack tip (Crone and Shield, 2001; Crone et al., 2004, 2003; Shield, 1996), as well as by our CPFE results that will be discussed.

We also analyze the angular sectors and associated active slip systems at a large radial distance $r = 150 \mu\text{m}$ ($30r_0$) for both (010)[101] and (101)[010] cracks. To achieve this, we extract the corresponding angular distribution of τ^α for the two crack orientations, as shown in Fig. 9a and b, respectively. The horizontal dashed lines indicate the critical magnitude of τ^α for the activation of each slip system, also set at 60 MPa. Based on Fig. 9a and b, we determine the arrangement of angular sectors along with the active slip systems in each sector for the two crack orientations, as shown in Fig. 9c and d, respectively. It should be noted that the results in Fig. 9c and d only represent the sector distributions around $r = 150 \mu\text{m}$ ($30r_0$), while straight sector boundaries are drawn up to the crack tip. Both Fig. 9c and d exhibit fewer plastic sectors covering smaller angular ranges when compared to the seven plastic sectors at $r = 70 \mu\text{m}$ ($14r_0$) in Fig. 8c and d. Correspondingly, the angular ranges expands for the elastic sectors. In addition, there is a new elastic sector

when θ exceeds 90° for the (010)[101] crack. These increased angular ranges of elastic sectors result from the overall decreased stresses as the radial distance r increases from the crack tip.

Based on the plastic sector distributions described above at various radial distances, we assemble the lobes of slip strain on different slip systems (Fig. 7) to establish crack tip plastic sectors for the two crack orientations, as depicted in Fig. 9e and f, respectively. Our focus lies particularly on type I and type II slip systems, because each of their associated $\langle 110 \rangle$ slip vectors possesses an out-of-plane component capable of generating observable slip traces on the specimen surface near the crack tip. This enables us to compare the

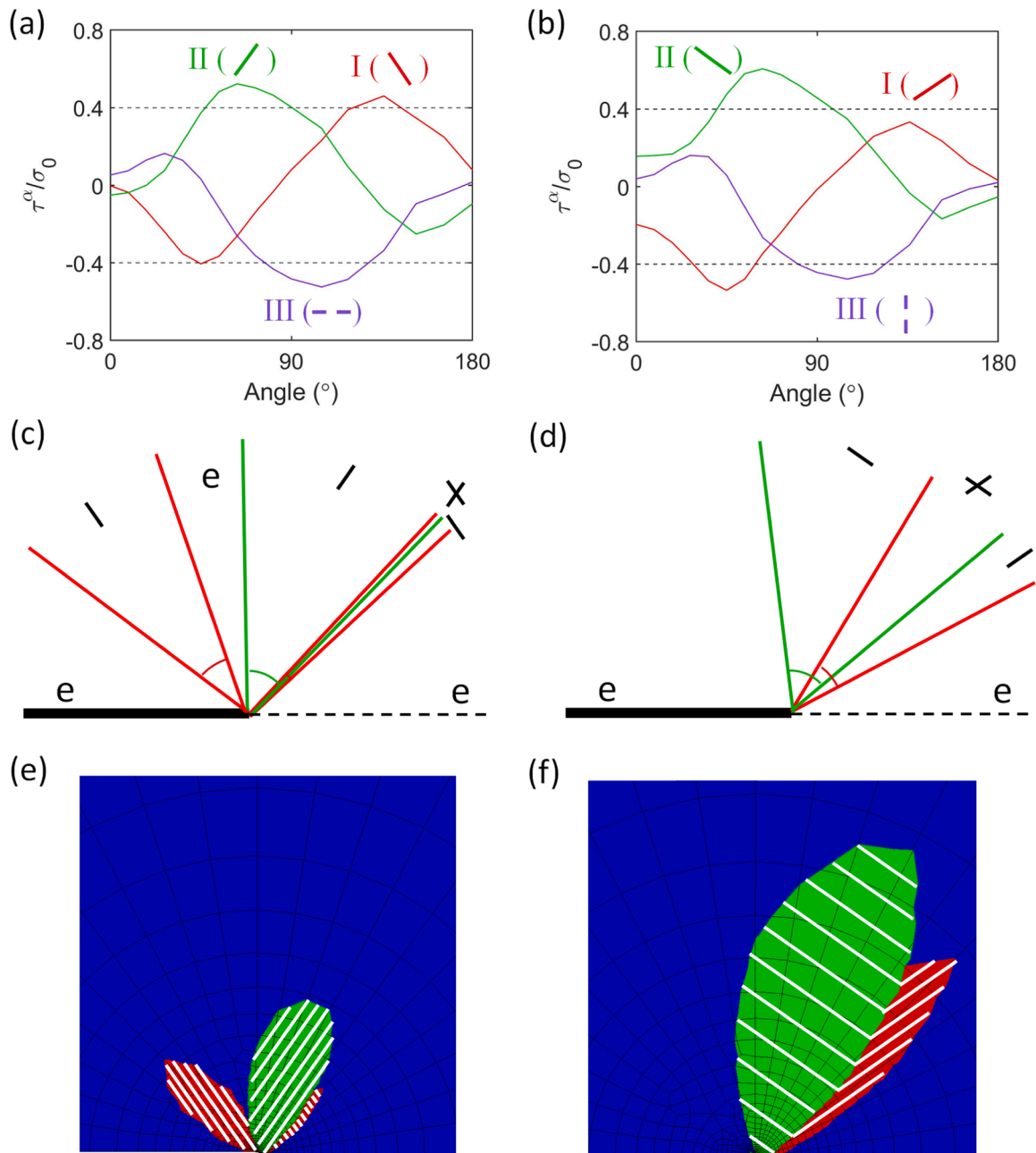


Fig. 9. Resolved shear stress and the arrangement of angular sectors of different active slip systems along an angular path with the radial distance $r = 150 \mu\text{m}$ ($30r_0$) for (010)[101] and (101)[010] cracks at $K = 15 \text{ MPa}\sqrt{\text{m}}$. (a-b) Angular distributions of resolved shear stress on the three types of active slip systems for the two crack orientations, respectively. (c-d) Sketch of the sector boundaries for the two crack orientations, respectively. Short black segments indicate slip plane orientations of the active single or double slip in each sector. (e-f) Simulated plastic sectors visible on the specimen surface near the crack tip, showing the curved sector boundaries as well as the traces (indicated by white lines) of primary slip within each sector associated with type I and type II slip systems for the two crack orientations, respectively. Multiple plastic sectors for each crack orientation are assembled based on the slip strain contours in Fig. 7a1-a2 and b1-b2, respectively.

simulated crack tip plastic sectors with experimental observations. In contrast, the $\langle 110 \rangle$ slip vector associated with type III slip systems lacks an out-of-plane component and thus cannot produce observable slip traces on the specimen surface near the crack tip. In addition, we note that in experimental observations (Crone et al., 2004; Shield, 1996), the plastic sectors primarily contained traces of single slip. This finding suggests that primary slip, under higher τ^c , tends to prevail over secondary slip in terms of producing slip traces on the specimen surface. Hence, when assembling the lobes of slip strain, we only consider the primary slip system when double slip is involved. Fig. 9e and f show the simulated plastic sectors featuring curved boundaries. Each sector is overlaid with the traces of primary slip associated with either type I or type II slip system for the two crack orientations, respectively. They closely align with the corresponding experimental observations of slip traces on the surface of cracked specimens of single crystal Cu (Crone et al., 2004; Shield, 1996). As discussed above, the $\langle 110 \rangle$ slip vector associated with type III slip systems cannot produce slip traces on the specimen surface near the crack tip. However, the slip traces corresponding to the slip planes of type III slip systems were observed in experiments (Crone et al., 2004). These traces likely resulted from the activation of other slip directions on the slip planes of type III slip systems. This is because these slip directions have out-of-plane components and are compatible with plane stress deformation near the specimen surface. Overall, our CPFEM simulations effectively capture the key characteristics of crack tip strain and stress fields in single crystals reported in previous studies. These CPFEM results bridge the gap between the asymptotic solutions and experimental observations, particularly in terms of the plastic sectors consisting of slip traces on the specimen surface near the crack tip. They can be utilized for the essential calibration of CPFEM modeling of crack tip plastic behavior in fcc crystals in the future.

3.3. Crack tip fields in single crystals under cyclic loading

We further analyze crack tip fields in the semi-circular single crystal domain (Fig. 2b) under cyclic loading. Fig. 10a shows the same cyclic loading profile of applied stress intensity factor K as Fig. 5a. Recall that the cyclic CP model used in this study exhibits a nearly stable stress-strain hysteresis loop by the third cycle (Fig. 1). As a result, our cyclic crack simulation can quickly approach a steady rate

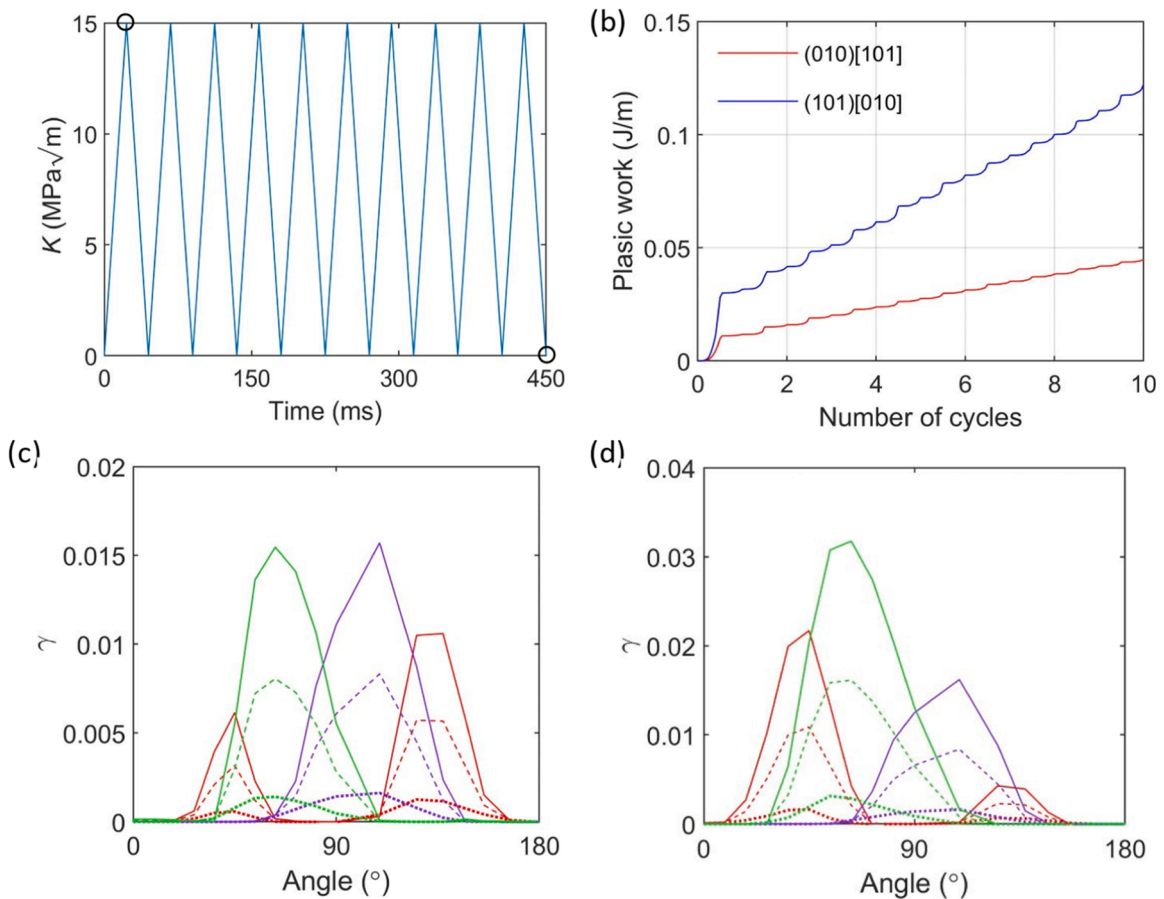


Fig. 10. Evolution of plastic work and slip strain for three types of active slip systems under cyclic loading. (a) Schematic of loading cycle at $\Delta K = 15 \text{ MPa}\sqrt{\text{m}}$. (b) Plastic work vs. number of cycles. (c) and (d) Angular distribution of slip strain at $r = 70 \mu\text{m}$ ($14r_0$) on type I (red curves), II (green curves) and III (purple curves) slip systems for (010)[101] and (101)[010] cracks, respectively, at three representative loads of K_{max} in the first cycle (dotted lines), K_{min} at the end of the 5th cycle (dashed lines), and K_{min} at the end of the 10th cycle (solid lines), as marked by circles in Fig. 10a.

value of dW_p/dN for each loading condition, which is used to determine the corresponding fatigue crack growth rate, once the value of w_p^c is calibrated to an experiment. The attainment of this steady rate is evident from Fig. 10b, where the accumulated plastic work W_p increases at an approximately constant rate dW_p/dN beyond the third cycle.

Fig. 10c and d show the angular distributions of slip strain γ on the three types of active slip systems at $r = 70 \mu\text{m}$ ($14r_0$) for the (010) [101] and (101)[010] cracks, respectively. These angular distributions correspond to three representative loads: K_{\max} in the first cycle, K_{\min} at the end of the 5th cycle, and K_{\min} at the end of the 10th cycle, as shown in Fig. 10a by dotted, dashed and solid lines, respectively. It is seen that γ on the three active slip systems increases with cycles. In Fig. 10c, corresponding to the (010)[101] crack, the angular distribution of γ on type I slip systems (red curves) exhibits two peaks at $\theta = 45^\circ$ and 134° at all three loads examined. These peaks indicate the accumulation of large γ over cycles along these two orientations. This is consistent with the large forward-leaning and backward-leaning lobes of γ (Fig. 7a1) observed in the first cycle. These lobes are elongated along $\theta = 45^\circ$ and 135° , respectively, indicating the occurrence of large γ along the two orientations. In contrast, the angular distribution of γ on type II slip systems (green curves) exhibits a single peak at $\theta = 63^\circ$, which indicates the accumulation of large γ over cycles along this orientation. This is consistent with the large forward-leaning lobe of γ (Fig. 7a2) observed in the first cycle, elongated along $\theta = 63^\circ$, indicating the occurrence of large γ along this orientation. Similarly, the angular distribution of γ on type III slip systems (purple curves) exhibits a single peak at $\theta = 109^\circ$, signifying the accumulation of large γ over cycles along this orientation. This is in line with the large upright lobe of γ (Fig. 7a3) observed in the first cycle, elongated along $\theta = 110^\circ$, indicating the occurrence of large γ along this orientation. A similar trend is observed from Fig. 10d for the (101)[010] crack, correlating to the large lobes of γ for the three types of active slip systems in Fig. 7b1-b3, respectively.

The cyclic plastic zones from cyclic CPFE simulations are also examined in Fig. 11 for the two crack orientations. The boundary of each stable cyclic plastic zone is estimated when the Mises stress reaches the nominal yield stress 150 MPa at the end of the 8th cycle. This is supported by Fig. 10b showing that the plastic work per cycle is nearly stabilized by the fifth cycle. The stable cyclic plastic zones in Fig. 11a and b reveal the effects of crystal anisotropy on their sizes and orientations. However, their sizes are consistent with that of the stable cyclic plastic zone at the end of the 8th cycle (Fig. 5e) from the cyclic JPF simulation.

3.4. Fatigue crack growth rates

The fatigue crack growth rate is determined for a range of loading levels using the method outlined in Section 2.6. To date, only a relatively limited number of studies (Aslan et al., 2011; Karamitros et al., 2022; Sakaguchi et al., 2019) have determined the fatigue crack growth rate based on CPFE modeling. Here, we evaluate the crack growth rate using cyclic CPFE simulations of stationary cracks as well as cyclic JPF simulations for comparison. Our study relies on accumulated plastic work as a criterion for fatigue crack growth, consistent in principle with a constant plastic work to failure of the damage process zone at each increment of crack growth. In Section 3.3, our comprehensive analysis of crack tip fields from CPFE simulations and comparison with experimental observations in the literature demonstrates the effects of crystallographic slip on crack tip stress and slip strain distributions. These effects can significantly influence the crack tip energy dissipation evaluated in terms of accumulated plastic work during cyclic loading, thereby impacting the simulated fatigue crack growth rate.

Fig. 12a and b show the accumulated plastic work W_p (calculated based on Eq. (19)) as a function of the number of cycles N from cyclic CPFE simulations for the two crack orientations under different ΔK , respectively. Fig. 12c shows the corresponding result of W_p (calculated based on Eq. (18)) vs. N from cyclic JPF simulations. In all three cases, dW_p/dN under a given ΔK stabilizes beyond the third cycle and remains an approximately constant subsequently, with the stabilized dW_p/dN increasing with ΔK . Evidently, dW_p/dN depends on crack orientation from cyclic CPFE simulations. For example, dW_p/dN is 0.0034 J/m and 0.01 J/m for the (010)[101] and (101)[010] cracks under $\Delta K = 15 \text{ MPa}\sqrt{\text{m}}$, respectively. These values contrast with $dW_p/dN = 0.0061 \text{ J/m}$ under the same ΔK from

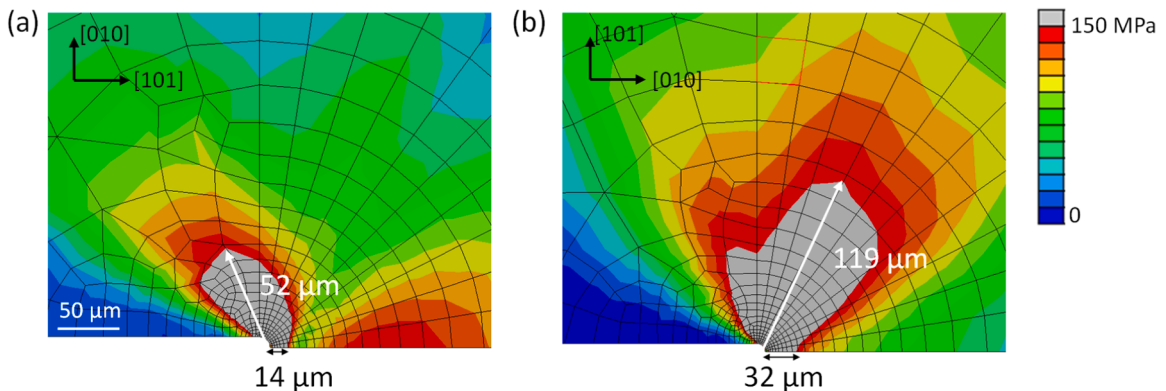


Fig. 11. Mises stress contours showing cyclic plastic zones for a cyclic load range $\Delta K = 15 \text{ MPa}\sqrt{\text{m}}$. (a) Contour of Mises stress for the (010)[101] crack at the end of the 8th cycle with $K_{\min} = 0$. A yield stress of 150 MPa is used as the upper limit of the stress contour, such that the region with grey color corresponds to the cyclic plastic zone. (b) Same as (a) except for the (101)[010] crack.

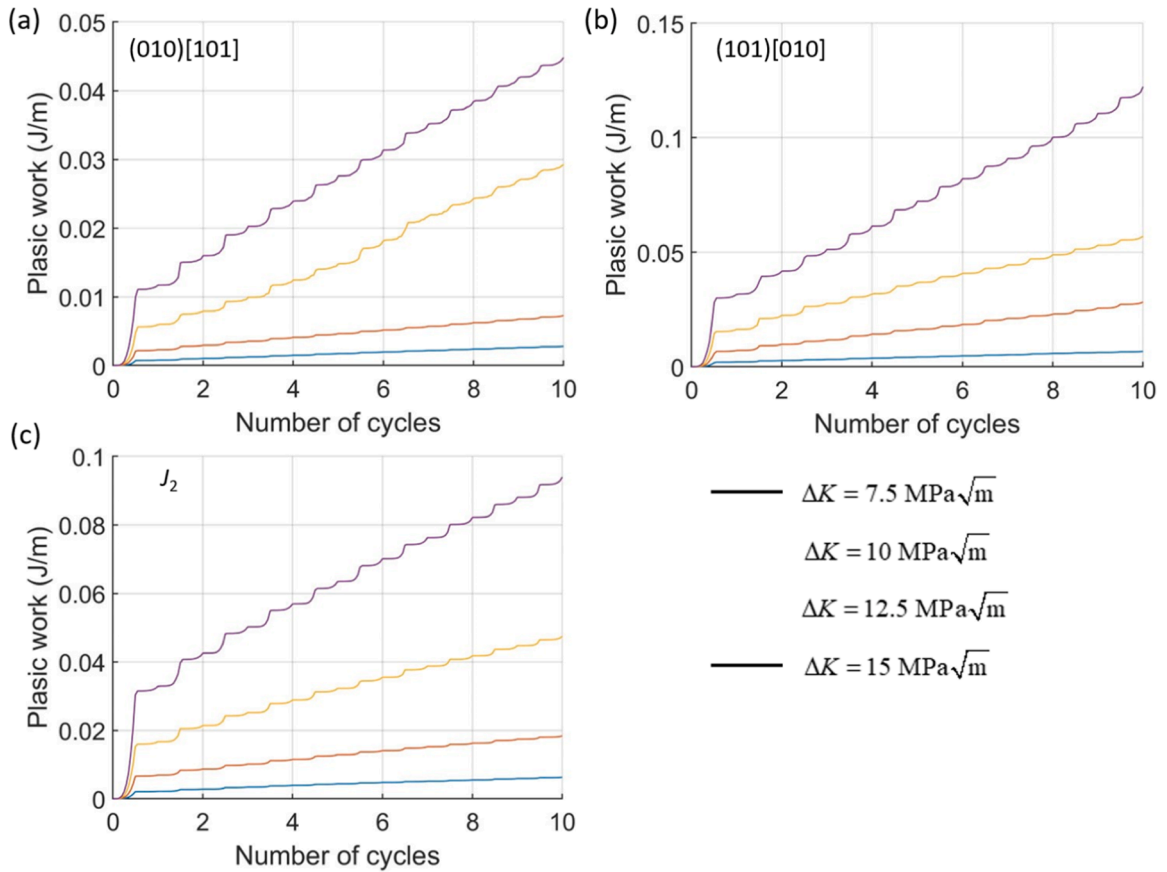


Fig. 12. Plastic work vs. number of cycles for different stress intensity ranges ΔK . (a) Cyclic CPFPE results for the (010)[101] crack. (b) Cyclic CPFPE results for the (101)[010] crack. (c) Cyclic JPFE results.

the cyclic JPFE simulation.

As discussed in Section 2.6, we use Eq. (24) to determine the Paris law expressing da/dN vs. ΔK . Besides the input of dW_p/dN , Eq. (24) requires the cyclic plastic zone size s and the critical plastic work density w_p^c . We estimate s from the averaged value of plastic zone sizes estimated along the crack propagation direction at the end of each cycle between the 4th and 10th cycles, during which the crack tip fields become stabilized. We fit w_p^c using the experimentally measured data of da/dN vs. ΔK . It should be emphasized that the Paris exponent m is a scaling exponent that makes contact with the scaling exponent in the present model which is independent of the fitted value of w_p^c ; in other words, the exponent in each case serves to scale da/dN with the underlying normalized driving force. To select the experimental data for fitting w_p^c , we note that several experiments on the measured fatigue crack growth rates in 316L stainless steel have been reported. For instance, Murakami and Matsuoka (Murakami and Matsuoka, 2010) conducted fatigue testing of 316L stainless steel at room temperature with a stress ratio $R = -1$ and testing frequencies of 1.5 Hz and 0.0015 Hz, respectively. The load range ΔK varied from 7 to 30 $\text{MPa}\sqrt{\text{m}}$. In addition, Lambert et al. (Lambert et al., 1988) performed fatigue crack propagation tests on CT specimens of 316 stainless steel at different R ratios. In our study, we use the experimental data from Murakami and Matsuoka at a testing frequency of 0.0015 Hz to fit w_p^c and further compare with our simulation results. This choice is made because the loading frequencies in our simulations are around 0.03 Hz. Although the R ratio differs between experiments and simulations, it has been shown that R has little influence on the exponent m in the Paris law (Huang and Moan, 2007).

In Fig. 13, we show the fatigue crack growth rates da/dN versus ΔK from the CPFPE simulations for single crystal 316L stainless steel with two crack orientations as well as by the JPFE simulations for polycrystalline 316L stainless steel. These simulated results are compared with experimental measurements (Murakami and Matsuoka, 2010). In the log-log plot of Fig. 13a and b, the CPFPE simulation results (red circles) closely align with the experimental data (black line) by expressing their corresponding da/dN values vs. ΔK . The Paris law of fatigue crack growth rate is shown by the linear curve (blue line) of da/dN vs. ΔK as fit to data in the log-log plot. Similarly, in Fig. 13c, the JPFE simulation results (red circles) and the associated fitting curve (blue line) exhibit close agreement with the experimental data (represented by a black line). The simulated Paris exponent m is respectively 3.17 and 3.00 for each of the two crack orientations based on CPFPE simulations and 2.81 based on JPFE simulations. When compared to the JPFE results, the CPFPE-simulated m values are closer to the experimentally measured m values of 2.91 and 3.27 at testing frequencies of 0.0015 Hz and 1.5 Hz, respectively (Murakami and Matsuoka, 2010). This closer agreement between CPFPE results and experimental measurements indicate

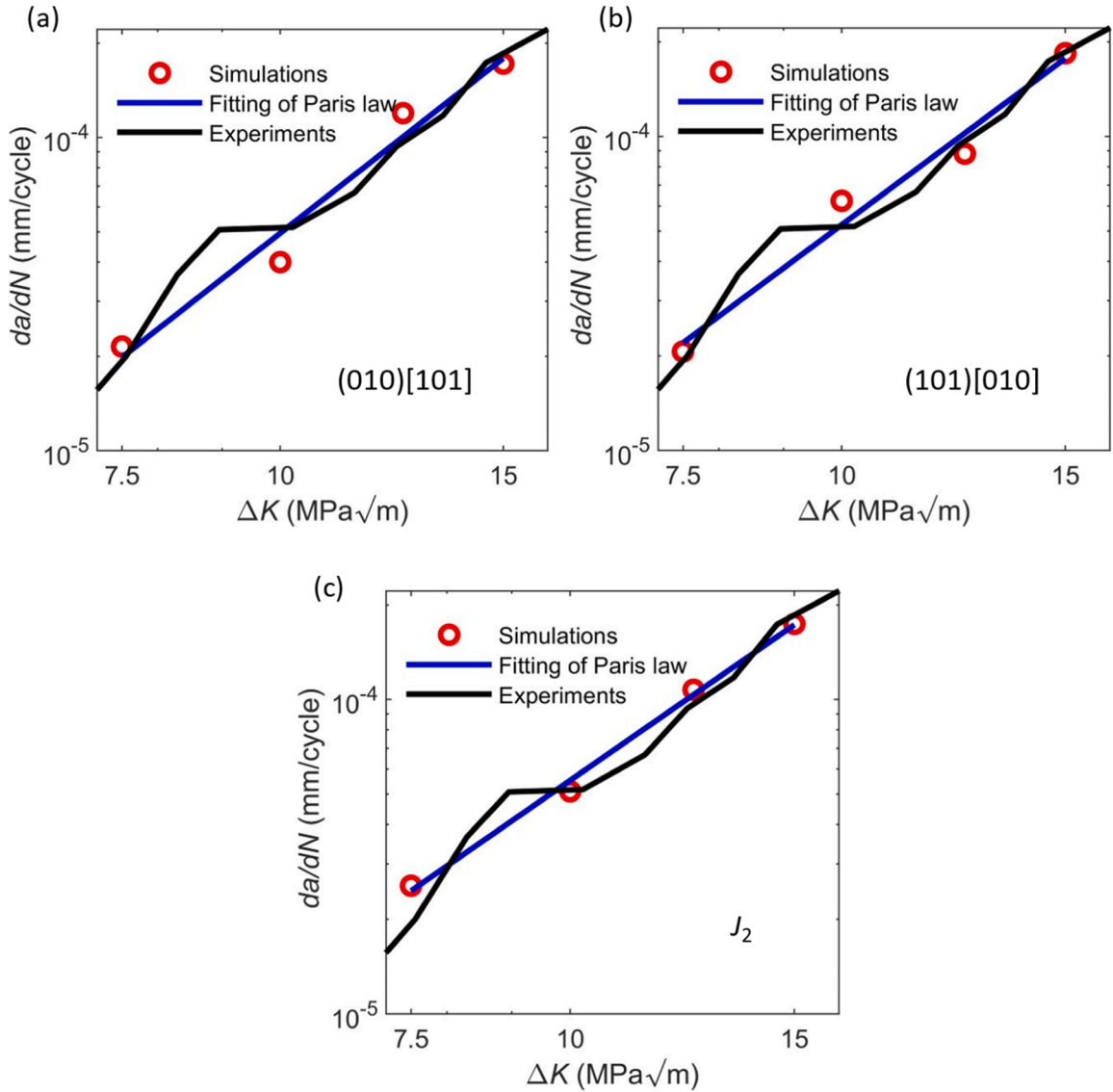


Fig. 13. Simulated fatigue crack growth rate versus stress intensity factor range ΔK (circles) as well as the fitted Paris law curve (blue line), as compared with the experimental Paris law curve (black line). (a) Cyclic CPFPE results for the (010)[101] crack. (b) Cyclic CPFPE results for the (101)[010] crack. (c) Cyclic JPFE results.

that cyclic CPFPE simulations can effectively capture key characteristics of crystallographic plastic slip near a crack tip, thereby improving the modeling of fatigue crack growth by considering such orientation effect.

We further note that Lambert et al. (Lambert et al., 1988) reported the experimentally measured crack growth rate of 316 stainless steel in terms of the cyclic J integral ΔJ , based on the growth rate relation $da/dN = C\Delta J^{m'}$. The experimentally measured exponent m' in this case is 1.55. Under the typical small-scale yielding condition, one can relate ΔJ and ΔK by $\Delta J = \frac{1-\nu^2}{E} \Delta K^2$. Then the corresponding Paris exponent m is $2m' = 3.1$. Hence, the CPFPE-determined m values are also consistent with the experimental m value by Lambert et al. (Lambert et al., 1988), which is expected since the cyclic plastic work per cycle is an effective surrogate measure for ΔJ . Moreover, Merah et al. (Merah et al., 1999) reported a Paris exponent m of 3.0 for 304 stainless steel with $R = 0$ and a test frequency of 1.0 Hz. Considering that 304 and 316L stainless steels are similar with only small percentage differences in alloying elements, these experimental results indicate that the Paris exponent should be around $m \approx 3$. Therefore, a combination of our cyclic CPFPE simulations and the fatigue crack growth criterion demonstrates the ability to evaluate fatigue crack growth rates.

As discussed in Section 2.6, the parameters w_p^c in Eq. (24) and C in Eq. (21) are coupled in expressing the scaling relation for fatigue crack growth rate as a function of driving force expressed by the Paris law. In Fig. 13, the value of C is determined by fitting the simulation data to the experimental measurements, resulting in different values of w_p^c as 0.23 J/mm² and 0.34 J/mm² for the two crack

orientations. During fatigue crack growth, newly formed crack surfaces have varying crystallographic orientations, which lead to different crack tip stresses, plastic strain fields, and mechanisms for irreversibility of the crack tip dislocations, consequently leading to different values of w_p^c . Hence, w_p^c understandably depends on crack orientation.

4. Conclusions

We have developed a CPFE model to simulate crack tip responses in crystalline solids under both monotonic and cyclic loading conditions. CPFE simulations under monotonic loading reveal deformation fields in fcc crystal grains near crack tips in 316L stainless steel for two different crack orientations. Our results are consistent with previous theoretical and experimental studies of crack tip deformation fields. From CPFE simulations under cyclic loading, a nonlocal critical plastic work criterion is employed to evaluate fatigue crack growth rates based on Eq. (24). These CPFE simulations closely correspond to cyclic JPFE simulations and previous experimental measurements. Our main findings are summarized as follows.

- Both cyclic CPFE and JPFE models account for nonlinear kinematic hardening to capture the pronounced Bauschinger effect in polycrystalline 316L stainless steel under cyclic loading. The cyclic stress-strain curves obtained from CPFE and JPFE simulations exhibit stable hysteresis loops that closely match experimental results in the literature. In addition to the Bauschinger effect, the CPFE model effectively represents the factors that influence deformation fields in crystal grains at the crack tip, including elastic and plastic anisotropies, finite strain, and finite lattice rotation.
- CPFE simulations of stationary cracks under monotonic loading provide detailed characterizations of deformation fields in crystal grains at the crack tip. These fields exhibit angular sectors with different active slip systems, resulting in distinct slip traces on the specimen surface near the crack tip. The CPFE results for angular sectors, considering two crystal grain orientations, are consistent with asymptotic solutions (Saeedvafa and Rice, 1989) and experimental observations (Crone et al., 2004).
- CPFE simulations of stationary cracks under cyclic loading show that slip strains on active slip systems and consequently the accumulated plastic work increase steadily over cycles following initial transients.
- The combination of cyclic CPFE simulations and the relation of da/dN in Eq. (24) enable determination of the fatigue crack growth rate as a function of stress intensity factor range for two orientations of crystal grains at the crack tip in 316L stainless steel. The simulated Paris law, including the Paris exponent, agrees with previous experimental measurements, which implies that our selected surrogate driving force is consistent with the fatigue damage process. CPFE simulations reveal the effects of crystallographic slip in crack tip crystal grains on fatigue crack growth.

It is worth noting that while our study focuses on crack tip fields and fatigue crack growth rates in a representative fcc alloy, 316L stainless steel, the CPFE modeling approach developed can be applied to bcc alloys. This applicability is supported by earlier asymptotic solutions showing close similarities of crack tip fields between fcc and bcc crystals (Rice, 1987). However, it is important to emphasize that our simulations of fatigue crack growth rates through cyclic CPFE are based on stationary cracks, which offer a computationally efficient approach compared to direct finite element simulations of fatigue crack growth processes. To address effects of growth history, future research should compare computational modeling results of stationary and growing cracks using the same constitutive model and crack setup, with experimental data as reference. Additionally, explicit modeling of polycrystalline grains at the crack front should be considered in future research.

Data availability

The data that support the findings of this study are available from the corresponding author upon request.

CRedit authorship contribution statement

Baolin Wang: Writing – original draft, Visualization, Validation, Methodology, Investigation, Formal analysis, Data curation, Conceptualization. **Yin Zhang:** Methodology, Investigation, Formal analysis, Conceptualization. **David L. McDowell:** Writing – review & editing, Supervision. **Ting Zhu:** Writing – review & editing, Supervision, Methodology, Investigation, Formal analysis, Conceptualization.

Declaration of competing interest

The authors declare that they have no known competing financial interests or personal relationships that could have appeared to influence the work reported in this paper.

Acknowledgements

We thank Drs. Theodore Zirkle and Tang Gu for their helpful discussions.

References

- ABAQUS/Explicit, 2009. User's Manual, Version 6.9. Dassault Systemes Simulia Corp, Providence, RI.
- Armstrong, P.J., Frederick, C.O., 1966. A mathematical representation of the multiaxial Bauschinger effect. CEGB Report RD/B/N 731. Central Electricity Generating Board.
- Asaro, R.J., Needleman, A., 1985. Overview no. 42 texture development and strain hardening in rate dependent polycrystals. *Acta Metall.* 33, 923–953.
- Aslan, O., Quilici, S., Forest, S., 2011. Numerical modeling of fatigue crack growth in single crystals based on microdamage theory. *Int. J. Damage Mech.* 20, 681–705.
- Bari, S., Hassan, T., 2000. Anatomy of coupled constitutive models for ratcheting simulation. *Int. J. Plast.* 16, 381–409.
- Castelluccio, G.M., McDowell, D.L., 2012. Assessment of small fatigue crack growth driving forces in single crystals with and without slip bands. *Int. J. Fract.* 176, 49–64.
- Castelluccio, G.M., McDowell, D.L., 2014a. A mesoscale approach for growth of 3D microstructurally small fatigue cracks in polycrystals. *Int. J. Damage Mech.* 23, 791–818.
- Castelluccio, G.M., McDowell, D.L., 2014b. Mesoscale modeling of microstructurally small fatigue cracks in metallic polycrystals. *Mater. Sci. Eng. A* 598, 34–55.
- Castelluccio, G.M., Musinski, W.D., McDowell, D.L., 2014. Recent developments in assessing microstructure-sensitive early stage fatigue of polycrystals. *Curr. Opin. Solid State Mater. Sci.* 18, 180–187.
- Chaboche, J.-L., 1986. Time-independent constitutive theories for cyclic plasticity. *Int. J. Plast.* 2, 149–188.
- Chaboche, J.-L., 1991. On some modifications of kinematic hardening to improve the description of ratchetting effects. *Int. J. Plast.* 7, 661–678.
- Cleveringa, H., Van der Giessen, E., Needleman, A., 2000. A discrete dislocation analysis of mode I crack growth. *J. Mech. Phys. Solids* 48, 1133–1157.
- Crone, W., Shield, T., 2001. Experimental study of the deformation near a notch tip in copper and copper–beryllium single crystals. *J. Mech. Phys. Solids* 49, 2819–2838.
- Crone, W., Shield, T., Creuziger, A., Henneman, B., 2004. Orientation dependence of the plastic slip near notches in ductile FCC single crystals. *J. Mech. Phys. Solids* 52, 85–112.
- Crone, W., Shield, T.W., 2003. An experimental study of the effect of hardening on plastic deformation at notch tips in metallic single crystals. *J. Mech. Phys. Solids* 51, 1623–1647.
- Cuitino, A., Ortiz, M., 1996. Three-dimensional crack-tip fields in four-point-bending copper single-crystal specimens. *J. Mech. Phys. Solids* 44, 863–904.
- Cuitino, A.M., Ortiz, M., 1993. Computational modelling of single crystals. *Model. Simul. Mat. Sci. Eng.* 1, 225–263.
- Deka, N., Jonnalagadda, K.N., 2017. Numerical investigation of crack tip strain localization under cyclic loading in FCC single crystals. *Int. J. Fract.* 204, 29–53.
- Drugan, W., 2001. Asymptotic solutions for tensile crack tip fields without kink-type shear bands in elastic-ideally plastic single crystals. *J. Mech. Phys. Solids* 49, 2155–2176.
- Fatemi, A., Socie, D.F., 1988. A critical plane approach to multiaxial fatigue damage including out-of-phase loading. *Fatigue Fract. Eng. Mater. Struct.* 11, 149–165.
- Flouriot, S., Forest, S., Caillaud, G., Köster, A., Rémy, L., Burgardt, B., Gros, V., Mosset, S., Delautre, J., 2003a. Strain localization at the crack tip in single crystal CT specimens under monotonous loading: 3D finite element analyses and application to nickel-base superalloys. *Int. J. Fract.* 124, 43–77.
- Flouriot, S., Forest, S., Rémy, L., 2003b. Strain localization phenomena under cyclic loading: application to fatigue of single crystals. *Comput. Mater. Sci.* 26, 61–70.
- Forest, S., Boubidi, P., Sievert, R., 2001. Strain localization patterns at a crack tip in generalized single crystal plasticity. *Scr. Mater.* 44, 953–958.
- Garrett, G., Knott, J., 1975. Crystallographic fatigue crack growth in aluminium alloys. *Acta Metall.* 23, 841–848.
- Glinka, G., 1982. A cumulative model of fatigue crack growth. *Int. J. Fatigue* 4, 59–67.
- Hassan, T., Kyriakides, S., 1992. Ratcheting in cyclic plasticity, part I: uniaxial behavior. *Int. J. Plast.* 8, 91–116.
- Hennessey, C., Castelluccio, G.M., McDowell, D.L., 2017. Sensitivity of polycrystal plasticity to slip system kinematic hardening laws for Al 7075-T6. *Mater. Sci. Eng. A* 687, 241–248.
- Hosseini, Z.S., Dadfarnia, M., Somerday, B.P., Sofronis, P., Ritchie, R.O., 2018. On the theoretical modeling of fatigue crack growth. *J. Mech. Phys. Solids* 121, 341–362.
- Huang, X., Moan, T., 2007. Improved modeling of the effect of R-ratio on crack growth rate. *Int. J. Fatigue* 29, 591–602.
- Hutchinson, J., 1968. Singular behaviour at the end of a tensile crack in a hardening material. *J. Mech. Phys. Solids* 16, 13–31.
- Jiang, Y.-Y., 2000. A fatigue criterion for general multiaxial loading. *Fatigue Fract. Eng. Mater. Struct.* 23, 19–32.
- Kalidindi, S.R., Bronkhorst, C.A., Anand, L., 1992. Crystallographic texture evolution in bulk deformation processing of FCC metals. *J. Mech. Phys. Solids* 40, 537–569.
- Karamitros, V., MacLachlan, D.W., Dunne, F.P., 2022. Mechanistic fatigue in Ni-based superalloy single crystals: a study of crack paths and growth rates. *J. Mech. Phys. Solids* 158, 104663.
- Kujawski, D., Ellyin, F., 1984. A fatigue crack propagation model. *Eng. Fract. Mech.* 20, 695–704.
- Kysar, J.W., Briant, C.L., 2002. Crack tip deformation fields in ductile single crystals. *Acta Mater.* 50, 2367–2380.
- Lambert, Y., Saillard, P., Bathias, C., 1988. Application of the J concept to fatigue crack growth in large-scale yielding. *ASTM STP* 969, 318–329.
- Liu, H.-W., Iino, N., 1969. A mechanical model for fatigue crack propagation. In: *Proc. 2nd Int. Conf. on Fracture*. Chapman-Hall, pp. 812–823.
- Lu, Y., Chen, Y., Zeng, Y., Zhang, Y., Kong, D., Li, X., Zhu, T., Li, X., Mao, S., Zhang, Z., Wang, L., Han, X., 2023. Nanoscale ductile fracture and associated atomistic mechanisms in a body-centered cubic refractory metal. *Nat. Commun.* 14, 5540.
- Majumdar, S., Morrow, J., 1974. Correlation between fatigue crack propagation and low cycle fatigue properties. *ASTM STP* 559, 159–182.
- Marchal, N., Flouriot, S., Forest, S., Rémy, L., 2006. Crack-tip stress–strain fields in single crystal nickel-base superalloys at high temperature under cyclic loading. *Comput. Mater. Sci.* 37, 42–50.
- McDowell, D., 1995. Stress state dependence of cyclic ratchetting behavior of two rail steels. *Int. J. Plast.* 11, 397–421.
- McDowell, D.L., 1996. Basic issues in the mechanics of high cycle metal fatigue. *Int. J. Fract.* 80, 103–145.
- McDowell, D.L., Berard, J.-Y., 1992. A δJ -based approach to biaxial fatigue. *Fatigue Fract. Eng. Mater. Struct.* 15, 719–741.
- McEvily Jr, A., Boettner, R., 1963. On fatigue crack propagation in FCC metals. *Acta Metall.* 11, 725–743.
- Merah, N., Bui-Quoc, T., Bernard, M., 1999. Notch and temperature effects on crack propagation in SS 304 under LCF conditions. *J. Pressure Vessel Technol.* 121, 42–48.
- Mohan, R., Ortiz, M., Shih, C., 1992. An analysis of cracks in ductile single crystals—II. Mode I loading. *J. Mech. Phys. Solids* 40, 315–337.
- Morrow, J., 1965. Cyclic plastic strain energy and fatigue of metals, internal friction, damping, and cyclic plasticity. *ASTM STP* 378, 45–87.
- Murakami, Y., Matsuoka, S., 2010. Effect of hydrogen on fatigue crack growth of metals. *Eng. Fract. Mech.* 77, 1926–1940.
- Nakatani, A., Kitagawa, H., Sugizaki, M., 1999. Discrete dislocation dynamics study of fracture mechanism and dislocation structures formed in mesoscopic field near crack tip under cyclic loading. *JSME Int. J. Ser. A* 42, 463–471.
- Neumann, P., 1974a. The geometry of slip processes at a propagating fatigue crack—II. *Acta Metall.* 22, 1167–1178.
- Neumann, P., 1974b. New experiments concerning the slip processes at propagating fatigue cracks-I. *Acta Metall.* 22, 1155–1165.
- Oh, K.P., 1978. A weakest-link model for the prediction of fatigue crack growth rate. *J. Eng. Mater. Technol.* 100, 170–174.
- Ohno, N., Wang, J.-D., 1993. Kinematic hardening rules with critical state of dynamic recovery, part I: formulation and basic features for ratchetting behavior. *Int. J. Plast.* 9, 375–390.
- Paris, P., Erdogan, F., 1963. A critical analysis of crack propagation laws. *J. Basic Eng.* 85, 528–533.
- Patil, S., Narasimhan, R., Mishra, R.K., 2009. Families of asymptotic tensile crack tip stress fields in elastic-perfectly plastic single crystals. *Int. J. Fract.* 155, 143–153.
- Patil, S.D., Narasimhan, R., Biswas, P., Mishra, R., 2008a. Crack tip fields in a single edge notched aluminum single crystal specimen. *J. Eng. Mater. Technol.* 130, 021013–021024.
- Patil, S.D., Narasimhan, R., Mishra, R., 2008b. A numerical study of crack tip constraint in ductile single crystals. *J. Mech. Phys. Solids* 56, 2265–2286.
- Peirce, D., Asaro, R.J., Needleman, A., 1983. Material rate dependence and localized deformation in crystalline solids. *Acta Metall.* 31, 1951–1976.

- Pham, M., Holdsworth, S., Janssens, K., Mazza, E., 2013. Cyclic deformation response of AISI 316L at room temperature: mechanical behaviour, microstructural evolution, physically-based evolutionary constitutive modelling. *Int. J. Plast.* 47, 143–164.
- Radon, J., 1982. A model for fatigue crack growth in a threshold region. *Int. J. Fatigue* 4, 161–166.
- Rice, J., Hawk, D., Asaro, R., 1990. Crack tip fields in ductile crystals. *Int. J. Fract.* 42, 301–321.
- Rice, J.R., 1987. Tensile crack tip fields in elastic-ideally plastic crystals. *Mech. Mater.* 6, 317–335.
- Rice, J.R., Rosengren, G.F., 1968. Plane strain deformation near a crack tip in a power-law hardening material. *J. Mech. Phys. Solids* 16, 1–12.
- Saeedvafa, M., Rice, J.R., 1989. Crack tip singular fields in ductile crystals with Taylor power-law hardening: II: Plane strain. *J. Mech. Phys. Solids* 37, 673–691.
- Sakaguchi, M., Komamura, R., Chen, X., Higaki, M., Inoue, H., 2019. Crystal plasticity assessment of crystallographic Stage I crack propagation in a Ni-based single crystal superalloy. *Int. J. Fatigue* 123, 10–21.
- Shield, T., 1996. An experimental study of the plastic strain fields near a notch tip in a copper single crystal during loading. *Acta Mater.* 44, 1547–1561.
- Shield, T., Kim, K.-S., 1994. Experimental measurement of the near tip strain field in an iron-silicon single crystal. *J. Mech. Phys. Solids* 42, 845–873.
- Sofronis, P., McMeeking, R.M., 1989. Numerical analysis of hydrogen transport near a blunting crack tip. *J. Mech. Phys. Solids* 37, 317–350.
- Suresh, S., 1998. *Fatigue of Materials*. Cambridge University Press, Cambridge, UK.
- Van der Giessen, E., Deshpande, V., Cleveringa, H., Needleman, A., 2001. Discrete dislocation plasticity and crack tip fields in single crystals. *J. Mech. Phys. Solids* 49, 2133–2153.
- Vehoff, H., Neumann, P., 1979. In situ SEM experiments concerning the mechanism of ductile crack growth. *Acta Metall.* 27, 915–920.
- Williams, M.L., 1957. On the stress distribution at the base of a stationary crack. *J. Appl. Mech.* 24, 109–114.
- Zhou, X., Li, X., Chen, C., 2015. Atomistic mechanisms of fatigue in nanotwinned metals. *Acta Mater.* 99, 77–86.
- Zirkle, T., McDowell, D.L., 2022. Analysis of monotonic and cyclic crack tip plasticity for a stationary crack tip in a FCC crystal. *Comput. Mater. Sci.* 202, 110954.